A bifunctional antibody targeting PD-1 and TGF-β signaling has antitumor activity in combination with radiotherapy and attenuates radiation-induced lung injury

Sheng Wang^{1,#}, Duo Xu^{1,#}, Yuan Wang¹, Yuehua Zhou², Lingyan Xiao¹, Fang Li¹, Jingyao Tu¹, Wan Qin¹, Sidan Tian³, Bolong Zheng⁴, Yihua Wang^{5, 6}, Xianglin Yuan^{1, *} Yuanhui Liu^{1, *} and Bo Liu^{1, *}

- 1. Department of Oncology, Tongji Hospital, Tongji Medical College, Huazhong University of Science and Technology, Wuhan 430030, Hubei, China
- 2. Top Alliance Biosciences Inc, Suzhou 215000, Jiangsu, China
- 3. National Engineering Research Center for Nanomedicine, College of Life Science and Technology, Huazhong University of Science and Technology, Wuhan 430074, Hubei, China.
- 4. School of Computer Science and Technology, Huazhong University of Science and Technology, Wuhan 430074, Hubei, China
- 5. Biological Sciences, Faculty of Environmental and Life Sciences, University of Southampton, Southampton SO17 1BJ, United Kingdom;
- 6. Institute for Life Sciences, University of Southampton, Southampton SO17 1BJ, United Kingdom.

#These authors contributed equally to the work.

*To whom correspondence should be addressed:

Xianglin Yuan, Department of Oncology, Tongji Hospital, Tongji Medical College, Huazhong University of Science and Technology, Wuhan 430030, Hubei, China. Telephone: 00-86-13667241722; Email: yuanxianglin@hust.edu.cn.

Yuanhui Liu, Department of Oncology, Tongji Hospital, Tongji Medical College, Huazhong University of Science and Technology, Wuhan 430030, Hubei, China. Telephone: 00-86-13342887209; Email: liuyuanhui23@tjh.tjmu.edu.cn.

Bo Liu, Department of Oncology, Tongji Hospital, Tongji Medical College, Huazhong University of Science and Technology, Wuhan 430030, Hubei, China. Telephone: 00-86-15927168582; Email: boliu888@hotmail.com.

Running title: Combination therapy of JS-201 and radiotherapy

Authors' disclosures

The authors declare that they have no conflicts of interest.

Funding information

This work was supported by the State Key Program of National Natural Science of China (Grant No. 82130092) for Xianglin Yuan and grants from the National Natural Science Foundation of China (Grant No. 81902619) and Knowledge Innovation Program of Wuhan-Shuguang Project (Grant No. 2022020801020447) for Bo Liu.

Abstract

Radio-immunotherapy has antitumor activity but also increased toxicity. JS-201 is a dual antibody targeting PD-1 and TGF- β signaling. We investigated the antitumour effect of JS-201 combined with radiotherapy and the effect on radiation-induced lung injury (RILI). Different tumor models were established to detect the antitumor effects of the combination of JS-201 and RT. RILI models were established to observe the effects of JS-201. Using transcriptome sequencing, We found that JS-201 optimized the TME through inhibiting extracellular matrix formation and angiogenesis. Combining JS-201 with radiotherapy further increased the inflammatory response and immune infiltration and showed great abscopal effects in LLC-luc models. Utilizing single-cell sequencing, we demonstrated that JS-201 reduced fibroblast proliferation by inhibiting the TGF- β /Smad pathway and the release of neutrophil extracellular traps mediated by ROS, thereby relieving radiation-induced pulmonary fibrosis. In conclusion, the JS-201 and radiotherapy combination enhances antitumor effects while mitigating acute and chronic RILI, and it may have potential for translational investigation as a cancer treatment strategy.

Synopsis

To overcome challenges experienced when combining radiotherapy with immune checkpoint inhibitors, the authors combined radiotherapy with a bifunctional antibody that inhibits PD-1 and TGF- β 1/2/3 simultaneously, finding it promotes antitumor activity, prolongs survival and reduces radiation-induced lung injury.

Introduction

The incidence and mortality rates of malignant tumors, especially thoracic tumors, are increasing every year, with breast cancer being the most common cancer worldwide and lung cancer being the deadliest (1). Radiotherapy (RT), an important therapy for thoracic tumors, has a bidirectional effect on the tumor immune microenvironment (TIME). Radiation-mediated DNA damage to tumor cells induces an increased type I/II IFN response to enhance innate immunity (2), while the death of immunogenic cells can release damage-associated molecular patterns (DAMPs) that induce the upregulation of MHC I/II and promote antigen presentation, thereby enhancing adaptive immunity (3, 4). In addition to the immune stimulatory effect, the expression of PD-L1 on the surface of tumor cells increases after RT, which activates the PD-1/PD-L1 pathway and leads to the exhaustion of cytotoxic T cells, resulting in immunosuppression (5).

Clinical application of immune checkpoint blockade (ICB) therapy has expanded rapidly in the last decade, but immune evasion mediated by the microenvironment of immune-excluded and immune-desert tumors has resulted in a low overall response to ICB therapy (6). Moreover, patients eligible for ICB therapy have poor survival benefits from immune checkpoint inhibitors (ICIs) (7). Based on the immunomodulatory effects of RT, the combination of RT and ICB is attracting attention, for example, increased PD-L1 expression in tumor cells after RT can activate the PD-1/PD-L1 signaling pathway, leading to depletion of effector T cells, which can be compensated by ICB. Moreover, the enhancement of antigen presentation triggered by RT exerts beneficial antitumor effects with ICB (8), and contributes to the abscopal effect (9). However, the normal tissue toxicity caused by combination therapy has become one of the main limitations of clinical application (10), especially the increased risk of acute/chronic radiation-induced lung injury (RILI) when combining thoracic RT with ICIs; for example, there was an increased incidence of pneumonitis in patients receiving anti-PD-L1 combined with RT within 90 days compared to those not receiving RT (13.6%) vs. 1.9%) (11). The PACIFIC study (12) also showed a trend toward a higher incidence of pneumonitis with sequential durvalumab (an anti-PD-L1) versus placebo after

chemoradiotherapy (33.9% vs 24.8%). Furthermore, a previous systemic review (13) reported that anti-PD-1/PD-L1 in combination with concurrent RT increased the risk of grade \geq 3 pneumonitis compared to sequential therapy (7.1% vs. 3.9%). Therefore, an important part of advancing immunotherapy development is overcoming the toxicity of combination therapy.

The TGF- β family plays an important role in a variety of pathophysiological processes through the activation of Smads by TGF- β receptors as well as various lineage-determining transcription factors (14). During tumor progression, the function of the TGF- β signaling pathway to suppress the immune response and promote epithelial-mesenchymal transition (EMT) can be hijacked by tumor cells, thereby facilitating tumor proliferation, migration and immune evasion (15). Moreover, TGF- β signaling plays a core role in RILI, which manifests as pneumonitis in the acute/subacute phase and fibrosis in the chronic phase, with a clinical incidence of 10-30% (16), impacting the advancement of treatment and patient prognosis. After radiation exposure, the latent-associated peptide–TGF- β complex deposited in the extracellular matrix (ECM) undergoes conformational changes induced by reactive oxygen species (ROS), releasing activated TGF- β signaling (17).

Due to the negative impact of TGF- β signaling on immunotherapy, the development of bifunctional antibodies targeting PD-L1 and TGF- β has received much attention. For example, apreclinical study confirmed the antitumour capacity of combination therapy with RT and M7824, a bifunctional antibody targeting PD-L1 and TGF- β simultaneously that is also known as bintrafusp alfa (18). Given that clinical trials reported the failure of single agent bintrafusp alfa in advanced NSCLC (19) and advanced/metastatic biliary tract cancers (20), combination with RT may play a critical role in the development of antitumour strategies that simultaneously target PD-L1 and TGF- β . However, superimposed toxic side effects have become a serious limitation of immuno-radiotherapy (21). Combined with the important role of TGF- β in RILI and the TIME, the combination of dual-targeted immune checkpoints and TGF- β signaling with RT may have therapeutic potential without increasing lung injury.

Bifunctional antibodies targeting PD-1 and TGF-β have been less studied

compared to PD-L1 and TGF- β , and no preclinical data have focused on the combination of RT and this kind of bifunctional antibody. Given the benefits of RT combined with ICB and the functions of TGF- β signaling, JS-201, an anti-mouse PD-1 antibody with the mouse TGF- β RII domain attached at the end to simultaneously target PD-1 and TGF- β signaling, was utilized in combination with RT in this study to explore a new opportunity for the integration of systemic and local treatment.

Materials and methods

Animals

Adult female C57BL/6 mice and BALB/c mice, 7-8 weeks old, weighing 18-20 g, were obtained from the Experimental Animal Center of Hubei Province and Hubei Biont Technology Co., Ltd. (Hubei, China). Under standard laboratory conditions, 5 mice per cage were fed sterile food and water ad libitum. All animal experiments were conducted under specific pathogen-free grade conditions in accordance with the guidelines of the International Guiding Principles for Animal Research and approved by the Ethics Committee of Huazhong University of Science and Technology (Hubei, China). The IACUC number is 3224.

Reagents

The mouse-derived bifunctional antibody JS-201 was provided by Shanghai Junshi Bioscience (Shanghai, China). The sequence of JS-201 is EVQLVESGGGLAQPGKSLKLSCEASGFTFSDYGMNWFRQAPGKGLEWVAYIS SGSNKITYADTVKGRFTVSRDNGKNQLFLQMNNLKSEDTAIYYCVDSGFNSY SDVWGQGIQVTVSSAKTTPPSVYPLAPGSAAQTNSMVTLGCLVKGYFPEPVT VTWNSGSLSSGVHTFPAVLQSDLYTLSSSVTVPSSTWPSETVTCNVAHPASSTK VDKKIVPRDCGCKPCICTVPEVSSVFIFPPKPKDVLTITLTPKVTCVVVDISKDD PEVQFSWFVDDVEVHTAQTQPREEQFNSTFRSVSELPIMHQDWLNGKEFKCR VNSAAFPAPIEKTISKTKGRPKAPQVYTIPPPKEQMAKDKVSLTCMITDFFPEDI TVEWQWNGQPAENYKNTQPIMDTDGSYFVYSKLNVQKSNWEAGNTFTCSV LHEGLHNHHTEKSLSHSPGAGGGGGGGGGGGGGGGGGGGGGGPPHVPKSDVE

MEAQKDASIHLSCNRTIHPLKHFNSDVMASDNGGAVKLPQLCKFCDVRLSTC DNQKSCMSNCSITAICEKPHEVCVAVWRKNDKNITLETVCHDPKLTYHGFTLE DAASPKCVMKEKKRAGETFFMCACNMEECNDYIIFSEEYTTSSPD. Mouse-derived anti-PD-1 (JS-001) and TGF-β trap (KLH-TGFβR2), which is constructed from a mouse-derived IgG antibody coupled to the TGF-β receptor II structural domain, were also provided by this company. JS-201 and JS-001 were diluted to 1 mg/ml with 0.9% sterile saline for in vivo experiments according to the manufacturer's instructions.

Cell lines and culture

All cell lines used in this research, including the Lewis lung cancer (LLC) cell line (TCM7), 4T1 breast cell line (TCM32) and CT26.WT colon cell line (TCM37), were obtained from the Cell Bank of Chinese Academy of Sciences (Shanghai, China) and authenticated to be of the correct strain and free of mycoplasma contamination by Short Tandem Repeats (STR) profiling and mycoplasma testing. The LLC luciferase-positive (LLC-luc) cell line was established from a parental LLC cell line by stable transduction with lentivirus containing luciferase GV260 obtained from Shanghai GeneChem Co., Ltd. (Shanghai, China). LLC and LLC-Luc cells were cultured in Dulbecco's modified Eagle's medium (HyClone, Utah, USA). CT26. WT and 4T1 cells were cultured in RPMI-1640 (HyClone). Cells were cultured in complete medium containing 10% fetal bovine serum (Gibco, New York, USA) and 1% penicillin–streptomycin (Gibco) and incubated with 5% carbon dioxide at 37°C. Cell passaging was performed twice per week when the cell density reached 80%-90%. All cells were used within 5 to 10 passages of thawing, and the cultivation never exceeded 1 month. All operations were performed at a super clean bench.

Murine model construction and treatment

Tumor-bearing models

For primary single-focal tumor experiments, LLC cells were inoculated subcutaneously into the right flank of C57BL/6 mice at a dose of 1×10^6 in 50 μ l. CT26 and 4T1 cells were inoculated into BALB/c mice at the same dose, and in the same location and

manner to establish different primary focal tumor models. Mice were divided randomly into the following 8 treatment groups with equal numbers in each group: 0.9% saline as the negative control (NC), anti-PD-1 (JS-001), TGF-β trap (KLH-TGFβR2), JS-201, RT-only (RT), anti-PD-1+RT, TGF-β trap+RT, and JS-201+RT. The experiments for the treatment of LLC and CT26 tumors were performed with 9 mice per group and 7 mice per group for 4T1. In the complementary experiments, mice were divided randomly into 4 groups as the anti-PD-1+TGF-β trap, JS-201, anti-PD-1+TGF-β trap+RT and JS-201+RT groups. The experiments for the treatment of LLC, CT26 and 4T1 tumors were performed with 6 mice per group.

Treatment was started when the primary tumor volume reached 100 mm³ approximately 7-10 days after inoculation. JS-201 and TGF-β trap were injected at a dose of 10 mg/kg while anti-PD-1 was injected at a dose of 8 mg/kg intraperitoneally at D0, D3, D6 and D9. For the RT, anti-PD-1+RT, TGF-β trap+RT, anti-PD-1+TGF-β trap+RT, and JS-201+RT groups, a dose of 8 Gy radiation targeting the tumor at D4 was implemented using an RS2000 X-ray Biological Research Irradiator (Rad Source Technologies, Suwanee, USA). Mice were placed on shelf 1 after anaesthesia with a source skin distance (SSD) of 501 mm and a dose rate of 1.214 Gy/min. The 2570/1 Farmer Dosemeter was utilized to conduct the dosimetry study. We fixed the single probe with the tumor, uncovered tissue adjacent to the tumor and covered abdomen separately for dose monitoring.

For the double tumor lesion experiment exploring abscopal effects, 1×10⁶ LLC-luc cells were inoculated into the right anterior flank of C57BL/6 mice as the primary tumor lesion, while 5×10⁵ LLC-luc cells were inoculated into the right posterior flank as the secondary lesion (n=10). RT was performed only on the primary site. Secondary tumors and normal tissues that were not irradiated were covered with lead plates. Tumor volume was measured every 3 days.

In this research, mice were euthanized when their tumor volume exceeded approximately 2,000 mm³ or the maximum diameter reached 15mm. The formula for calculating the tumor volume was Volume= Length \times Width²/2. We measured the length and width of tumours by vernier callipers.

Radiation-indecued pulmonary fibrosis (RIPF) models

Adult female C57BL/6 mice were fixed after anaesthesia and placed on shelf 1 of an RS2000 X-ray Biological Research Irradiator with a source skin distance (SSD) of 501 mm and a dose rate of 1.214 Gy/min. Normal tissues that were not irradiated were covered with lead plates. The mice were randomly and equally divided into four groups: the NC group, RT group, anti-PD-1 group and JS-201 group. The mice in the NC group were not irradiated or treated. After a 16 Gy/1F dose of whole thoracic irradiation in all other groups, treatment was given periodically.

In the acute/subacute RIPF trial, a 10 mg/kg dose of JS-201 and an 8 mg/kg dose of anti-PD-1 were administered intraperitoneally on D0, D3, D6 and D9 after RT to be consistent with the treatment mode in the tumor-bearing models. Mice (n=15) were observed and evaluated separately at 1, 2 and 3 months after RT. For RNA sequencing, another set of acute RILI mice (n=9) was euthanized 1 month after RT. Both modelling and treatment were consistent.

In the chronic RILI trial, treatment was given every two weeks from week 13 to week 26 after completion of the acute/subacute phase administration. Body weight and survival of the mice (n=15) were recorded weekly, and the observation endpoint was set at week 26, i.e., 6 months after RT.

In vivo imaging

Tumor-bearing mice were anesthetized with 1.5% pentobarbital after intraperitoneal injection of D-luciferin potassium from Meilunbio (MB1834, Shanghai, China) at a dose of 10 μl/g and a concentration of 15 mg/ml. Fluorescence live imaging was detected and analyzed by an IVIS Spectrum Imaging System (Calliper Life Sciences, Massachusetts, USA). The exposure time was 15 seconds. Filter sets were fixed with the following parameters: excitation wavelength at 640 nm and emission wavelength at 670 nm. Acquired images were measured and analyzed by the Living Imaging software.

Micro-CT scan

Mice in the RIPF experiments were anesthetized with 1.5% pentobarbital and fixed in

the proper posture. Thorax computed tomography (CT) was scanned and reconstructed by a micro-CT scanner (SkyScan 1176, Bruker, Massachusetts, USA) to evaluate lung inflammation and fibrosis.

Enzyme-linked immunosorbent assays (ELISAs)

Target binding assay for JS-201

ELISAs were performed to determine the ability of JS-201 to bind PD-1 and TGF- β 1/TGF- β 2/TGF- β 3 separately and simultaneously. IgG antibody, anti-PD-1 (JS-001) and TGF- β trap (KLH-TGF β R2) were set as control.

For single target binding assays, PD-1 (RP01170, ABclonal, Hubei, China)/TGF-β1 (RP02523, ABclonal)/TGF-β2 (RP00672, ABclonal)/TGF-β3 (RP00645, ABclonal) proteins were embedded in high affinity plates overnight, washed, sealed and incubated with the antibody to be tested. The encapsulated concentration, PD-1 and TGF-β1/2/3, was 100ul per well at a concentration of 1ug/ml, and the amount per well was 100ng. Antibodies tested were set up on a concentration gradient from 10⁻¹ to 10⁶ ng/ml. After washing, HRP-conjugated anti-hIgG secondary antibody (YP382434, Upingbio) was added, and after incubation, chromogenic substrate (YP542632, Upingbio) was added. Color development was terminated with hydrochloric acid, and absorbance was detected at 450 nm using Thermo Scientific Varioskan LUX.

For dual-target binding assays, double sandwich ELISAs were performed. TGF- β 1/2/3 was 100ul per well at a concentration of 1ug/ml, and the amount per well was 100ng. TGF- β was embedded in high affinity plates overnight. After washing and sealing, the antibody to be tested was set up on a concentration gradient from 10^{-1} to 10^6 ng/ml and incubated. The plates were then washed, biotin-labelled (10377-H08H, Sino Biological) PD-1 protein was added, and the plates were incubated. The plates were washed and incubated with peroxidase-conjugated streptavidin (SA-HRP, YP284723, Upingbio). Simultaneous binding of JS-201 to TGF- β and PD-1 is indicated by absorbance values according to the standard ELISA protocol.

Cytokine assay

ELISAs were applied to quantify the expression of TGF-β1 and the MPO-DNA complex in mouse serum and bronchoalveolar lavage fluid to reflect the content of NETs. The experimental procedure was performed using MPO-DNA complex (MM-1177M2, Meimian, Jiangsu, China) and TGF-β1 (EK981, Multi Science, Hangzhou, China) ELISA kits according to the manufacturer's instructions. Absorbance was detected at 450 nm using Thermo Scientific Varioskan LUX.

Flow Cytometry (FCM)

Primary tumors, secondary tumors and spleens were dissected from euthanized mice for assessment of the distribution of immune cells in the tumor microenvironment using FCM (n=3). Tissues were minced and digested with collagenase type IV (bs165, Biosharp), hyaluronidase (bs171, Biosharp) and DNase (bs137, Biosharp) at 37°C for 1 hour. After rinsing and filtration, erythrocyte lysates were added to tumor tissues, centrifuged (1200 rpm, 5 min) and resuspended in PBS as cell suspensions. For panel 1 to assess CD4⁺ and CD8⁺ T cells, BV510 Zombie AquaTM Fixable Viability Kit (423101, BioLegend, California, USA), APC/CY7 anti-mouse CD45 (103115, BioLegend), PE anti-mouse CD3 (100205, BioLegend), BV421 anti-mouse CD4 (116023, BioLegend) and PerCP/CY5.5 anti-mouse CD8a (100733, BioLegend) were used for staining. For panel 2 to assess MDSCs and Tregs, APC/CY7 Zombie Aqua™ Fixable Viability Kit, BV510 anti-mouse CD45 (103138, BioLegend), PE anti-mouse CD3, BV605 anti-mouse CD4 (100547, BioLegend), PerCP/CY5.5 anti-mouse CD8a, APC anti-mouse CD25 (102011, BioLegend), BV421 anti-mouse FOXP3 (126419, BioLegend), FITC anti-mouse CD11b (101205, BioLegend) and PE/CY7 anti-mouse Ly-6G/Ly-6C (108416, BioLegend) antibodies were used for cell staining. FcR was blocked with anti-mouse CD16/32 (101320, BioLegend). Cell surface staining fixation and rupture of membranes were performed using a FCM kit (00-5523-00, Thermo Fisher). FCM was performed using a CytoFLEX LX (Beckman, California, USA) and analyzed using FlowJo v10.8.1 software.

Hydroxyproline (HYP) content assay

The HYP content in lung tissue was detected to reflect the metabolism of collagen in fibrotic lesions. The detection process strictly followed the instructions of the kit from Nanjing Jiancheng Bioengineering Institute (A030-2-1, Nanjing, China). Three mice from each group were randomly selected to remove a portion of lung tissue for detection, and two auxiliary wells were made. Absorbance was detected at 450 nm using Thermo Scientific Varioskan LUX.

Histopathology and immunohistochemistry (IHC)

Intact excised LLC tumors of tumor-bearing models and lung tissue of RIPF models were fixed in 4% paraformaldehyde for 24-48 hours. The tissues were then dehydrated in ethanol, embedded in paraffin, and cut into 4-µm-thick sections. Before staining, paraffin sections were deparaffinized in xylene, anhydrous ethanol, and 75% alcohol in that order and then rinsed with distilled water.

HE (BH0001), Masson (BH0002) and picrosirius red (B00039) staining kits were all purchased from Powerful Biology (Hubei, China). Pathological staining was performed using the corresponding kits according to the manufacturer's instructions. Picrosirius red sections were observed under a polarized light microscope (The microscope model: NIKON Eclipse ci; Software: NIS_F_Ver43000_64bit_E; Imaging system: NIKON digital sight DS-FI2.). Ashcroft score criteria were applied to HE staining of lung tissue from RIPF models to assess the severity of fibrotic lesions in the different treatment groups. ImageJ was used for visual quantitative analysis.

For IHC experiments, after antigen retrieval, 3% hydrogen peroxide blocking, and 3% BSA sealing, sections were incubated with the following primary antibodies: anti-CAMK2A (1:800, A22611, ABclonal, Hubei, China), anti-CD8 (1:1000, ab217344, Abcam, Cambridge, UK), anti-CD31 (1:2000, ab182981, Abcam) and anti MPO (1:1000, GB11224, Servicebio, Hubei, China). Following secondary antibody (ab6789, Abcam) incubation, sections were developed with DAB (DA1010, Solarbio) and stained for nuclei with hematoxylin (GC307020, Servicebio) before dehydration and

sealing. Images were captured with a general microscope (ICX41, SDPTOP, Shanghai, China) and the Lightools software.

Immunofluorescence (IF)

Frozen lung tissue and BALF from RIPF models were sectioned at 4 μ m. DHE staining was performed using a Reactive Oxygen Species Assay Kit (S0033S, Beyotime, Shanghai, China) and DAPI staining solution (B0025, Powerful Biology) according to the manufacturer's instructions.

Lung tissue from RIPF models fixed with 4% paraformaldehyde was embedded in paraffin, sectioned at 4 μm, deparaffinized and rinsed. Homologous double-labeled IF was performed using anti-histone H3 (citrulline R2 + R8 + R17, CITH3) antibody (1:2000, ab281584, Abcam) and anti-MPO antibody (1:1000, GB11224, Servicebio) as primary antibodies. At the end of the secondary antibody (CY3 Labeled Goat Anti-Rabbit IgG, 1:300, GB21303, Servicebio; Alexa Fluor 488 Labeled Goat Anti-Rabbit IgG, 1:400, GB25303, Servicebio) incubation, cellular nuclei were stained with DAPI (G1401, Servicebio), and sections were sealed after removal of tissue autofluorescence.

DAPI excitation wavelength 330-380nm, emission wavelength 420nm; The excitation wavelength of 488 is 465-495nm, and the emission wavelength is 515-555nm. The excitation wavelength of CY3 is 510-560 nm, and the emission wavelength is 590nm. The excitation wavelength of CY5 is 608-648nm, and the emission wavelength is 672-712 nm. Pannoramic MIDI (3DHISTECH) was used for digital slide scanning. CaseViewer was used for image acquisition.

Quantitative PCR (qPCR)

RNA was extracted from total LLC tumor tissue using Trizol (G3013, Servicebio). Subsequently, 1000 ng of the obtained RNA was added and reverse-transcribed to cDNA using HiScript II Q RT SuperMix (R222-01, Vazyme, Nanjing, China). 3 subwells were set up for each assayed gene. Quantitative PCR was performed using a qPCR system (q225, KUBO Technology, Beijing, China), for which 1 µl of the reverse transcription product was added. The mRNA expression levels of target genes were

normalized to β -actin expression levels using $2^-\Delta\Delta CT$ method.

The gene-specific primers used are as follows: β -actin, 5'-

GGCTGTATTCCCCTCCATCG-3'(forward),5'-CCAGTTGGTAACAATGCCATGT-

3'(reverse); Ccl5,5'-CTCCAATCTTGCAGTCGTGTTTG-3'(forward),5'-

ACCCTCTATCCTAGCTCATCTCC-3'(reverse); Colla1,5'-

TTCTGCCCGGAAGAATACGTATC-3'(forward),5'-

GGACATCTGGGAAGCAAAGTTTC-3'(reverse); Colla2,5'-

ACACAAGGAGTCTGCATGTCTAA-3'(forward),5'-

TCGTACTGATCCCGATTGCAAATA-3'(reverse); Col6a6,5'-

GACTCAGTACAGGGAAGGAATGG-3'(forward),5'-

CTTTCGCCCAGGAATGCTTTAAG-3'(reverse); Cxcl2,5'-

ACTGAACAAAGGCAAGGCTAACT-3'(forward),5'-

ACATAACAACATCTGGGCAATGG-3'(reverse); Cxcl3,5'-

AAGATACTGAAGAGCGGCAAGTC-3'(forward),5'-

AGCAGGTAAAGACACATCCAGAC-3'(reverse); Cxcl10,5'-

GTGTTGAGATCATTGCCACGATG-3'(forward),5'-

TCAGAAGACCAAGGGCAATTAGG-3'(reverse); Illb, 5'-

CAGCACATCAACAAGAGCTTCAG-3'(forward),5'-

GAGGATGGGCTCTTCTTCAAAGA-3'(reverse); Itga8,5'-

GTGGACTGTGGAGAAGACAATCT-3'(forward),5'-

TTGCGCTCAATCCCAACATAATC-3'(reverse); *Itgb4*,5'-

GAGAATCCCAGCCATACCGATAC-3'(forward),5'-

TCTGGGATGATAGGGATGGACAT-3'(reverse).

Quantitative antibody detection

The quantification of JS-201 was conducted using sodium dodecyl sulfate—polyacrylamide gel electrophoresis (SDS-PAGE). Separation and concentration gels were added sequentially between the glass plates. Dithiothreitol (DTT) was used to revert the disulfide bond of JS-201. Then, JS-201 was mixed with the buffer and loaded. Electrophoresis was started at a constant voltage of 90 V. When bromophenol blue

started to penetrate the separating gel, the voltage was increased to 120 V. After electrophoresis, the gel was separated, stained and decoloured using Coomassie Brilliant Blue staining standards and then photographed by a gel imaging system (AlphaImager HP, Alpha Innotech, USA).

Western blot

Unfixed lung tissue from RIPF model mice was utilized for protein extraction. Lung tissue was added to RIPA buffer (G2002, Servicebio) and PMSF (G2007, Servicebio), crushed, subjected to ultrasonic shock and centrifugation, and boiled with 5 × loading buffer (G2013, Servicebio) at 100°C. A One-Step PAGE Gel Fast Preparation Kit (12%) (E304-01, Vazyme) was applied for electrophoresis. Protein bands were transferred to a polyvinylidene fluoride (PVDF) membrane (Millipore, Billerica, Massachusetts, USA) and blocked with 5% BSA or fat-free milk for 1 hour. PVDF membranes were incubated with the following primary antibodies at 4°C overnight: anti-COL3A1 (1:1000, 66887S, CST, Massachusetts, USA), anti-COL1A2 (1:1000, A5786, ABclonal), anti-Smad2 (1:1000, ab40855, Abcam), anti-phospho-Smad2 (Ser467) (1:1000, ab280888, Abcam), anti-GAPDH (1:10000, A00227-1, Boster, Hubei, China), anti-CAMK2A (1:1000, A22611, ABclonal), anti-α-SMA (1:1000, A17910, ABclonal), anti-TGF-β1 (1:1000, A2124, ABclonal) and anti-CITH3 (1:1000, ab281584, Abcam). After incubation with the appropriate secondary antibody (The secondary antibody for GAPDH is HRP-conjugated Goat anti-Mouse IgG (H+L), 1:10000, AS003, ABclonal. The secondary antibody for other antibodies is HRP-conjugated Goat anti-Rabbit IgG, 1:10000, AS014, ABclonal.) for 1 hour at room temperature, protein bands were visualized using Super Signal West Pico Chemiluminescent Substrate (Thermo Scientific, Massachusetts, USA). The signal of the blots was detected using the G: BOX Chemi X system (Syngene, Cambridge, UK).

RNA-seq assay

The sequenced tissues were mouse LLC tumour tissue and whole lung tissues 1 month after RT, using the same methods. RNA was extracted using the TRIzol lysate (RNAiso

Plus, 9109, TARAKA). Total RNA was treated with RQ1 DNase (M6101, Promega, Beijing, China) to remove DNA. The quality and quantity of the purified RNA were determined by measuring the absorbance at 260 nm/280 nm using SmartSpec Plus. RNA integrity was further verified by 1.5% agarose gel electrophoresis. For each sample, 1 µg of total RNA was used for RNA-seq library preparation. mRNAs were captured by VAHTS mRNA capture beads (N401, Vazyme). The purified RNA was treated with RQ1 DNase to remove DNA before being used for directional RNA-seq library preparation with the VAHTS Universal V8 RNA-seq Library Prep Kit for Illumina (NR605, Vazyme). Polyadenylated mRNAs were purified and fragmented. Fragmented mRNAs were converted into double-stranded cDNA. Following end repair and A tailing, the DNAs were ligated to an adaptor (N323, Vazyme). After purification of the ligation product and size fractionation to 300-500 bp, the ligated products were amplified and purified, quantified and stored at -80°C before sequencing. The strand marked with dUTP was not amplified, allowing strand-specific sequencing. For highthroughput sequencing, the libraries were prepared following the manufacturer's instructions and applied to an Illumina NovaSeq 6000 system (Illumina, USA) for 150 nt paired-end sequencing. Raw reads containing more than 2-N bases were first discarded. Then adaptors and low-quality bases were trimmed from raw sequencing reads using FASTX-Toolkit (Version 0.0.13). The short reads less than 16nt were also dropped. After that, clean reads were aligned to the GRCm39 M27 genome by HISAT2 allowing 4 mismatches. Uniquely mapped reads were used for gene reads number counting and FPKM calculation (fragments per kilobase of transcript per million fragments mapped). The R Bioconductor package DESeq2 was utilized to screen out the differentially expressed genes (DEGs). The P value <0.05 and fold change>2 or < 0.5 were set as the cut-off criteria for identifying DEGs.

Bioinformatics analysis

Processed RNA sequencing (RNA-seq) data of 6 control animal lung tissues and 24 irradiated animal lung tissues contained in the dataset GSE174196 was downloaded from the Gene Expression Omnibus (GEO) website

(https://www.ncbi.nlm.nih.gov/geo/). Differentially expressed genes (DEGs) between the control and irradiated lung tissues were identified with the R package "limma". Genes with $|\log 2(\text{fold-change})| > 1$ and adjusted P < 0.05 were considered as DEGs. T-test was used to evaluate the difference in transcription level of ATP2A1 and CASQ1 between normal and irradiated lung tissues. R software (version 4.4.0) (http://www.R-project.org/) was used for data analysis and figure plotting.

Single-cell RNA-seq assay

Cell preparation

10x Genomics® Cell Preparation Guide describes best practices and general protocols for washing, counting and concentrating cells from both abundant and limited cell suspensions in preparation for use in 10x Genomics Single Cell Protocols.

Single-Cell RNA Sequencing (scRNA-seq)

The cell suspension was loaded into Chromium microfluidic chips with 3' (v2 or v3, depends on project) chemistry and barcoded with a 10× Chromium Controller (10X Genomics). RNA from the barcoded cells was subsequently reverse-transcribed and sequencing libraries constructed with reagents from a Chromium Single Cell 3' v2 reagent kit (10X Genomics) according to the manufacturer's instructions. Sequencing was performed with Illumina NovaSeq 6000 according to the manufacturer's instructions (Illumina).

Quality control

We use fastp to perform basic statistics on the quality of the raw reads. Cellranger count support FASTQ files from raw base call (BCL) files generated by Illumina sequencers as input file. 10x Genomics® not recommend additional processing of the sequence.

Generation and Analysis of Single-Cell Transcriptomes

Raw reads were demultiplexed and mapped to the reference genome by 10X Genomics Cell Ranger pipeline (https://support.10xgenomics.com/single-cell-geneexpression/software/pipelines/latest/what-is-cell-ranger) using default parameters. All downstream single-cell analyses were performed using Cell Ranger and Seurat. For each gene and each cell barcode (filtered by CellRanger), unique molecule identifiers

were counted to construct digital expression matrices. Secondary filtration by Seurat: A gene with expression in more than 3 cells was considered as expressed, and each cell was required to have at least 200 expressed genes. And filter out some of the foreign cells.

Secondary Analysis of Gene Expression

Cellranger

Cellranger reanalyze takes feature-barcode matrices produced by cellranger count or cellranger aggr and reruns the dimensionality reduction, clustering, and gene expression algorithms using cellranger default parameter settings.

Seurat

The Seurat package was used to normalise data, dimensionality reduction, clustering, differential expression. we used Seurat alignment method canonical correlation analysis (CCA) for integrated analysis of datasets. For clustering, highly variable genes were selected and the principal components based on those genes used to build a graph, which was segmented with a resolution of 0.6.

Global Analysis Between Samples

Based on filtered gene expression matrix by Seurat ,between samples differential expression analysis was carried out using the edgeR package to obtain zone-specific marker genes.

Enrichment analysis of marker genes

Gene Ontology (GO) enrichment analysis of marker genes was implemented by the clusterProfiler R package, in which gene length bias was corrected. GO terms with corrected Pvalue less than 0.05 were considered significantly enriched by marker gene.

KEGG (Kanehisa M, 2008) is a database resource for understanding high-level functions and utilities of the biological system, such as the cell, the organism and the ecosystem, from molecular-level information, especially large-scale molecular datasets generated by genome sequencing and other high-through put experimental technologies (http://www.genome.jp/kegg/). We usedclusterProfiler R package to test the statistical enrichment of markergenes in KEGG pathways.

Reactome pathway-based analysis of marker genes was implemented by the ReactomePA R package. REACTOME is an open-source, open access, manually curated and peer-reviewed pathway database(https://reactome.org/)

In vivo biosafety evaluation

ALT, AST and Cr in the serum of mice in all treatment groups were detected to assess the effects of JS-201 on liver and kidney function by a Chemray 240 Automatic Biochemical Analyzer (Rayto Science, Shenzhen, China). Hearts, livers and kidneys of mice treated with JS-201 were fixed with 4% paraformaldehyde, sectioned and HE stained to observe the effect of JS-201 on vital organs.

Statistical analysis

Data were analyzed using GraphPad Prism version 8.0. The results are presented as the mean \pm standard deviation (SD) or standard error of the mean (SEM). Comparisons between two groups were made using Student's t test, and analysis between multiple groups was performed by one-way analysis of variance (ANOVA). Two-way ANOVA was selected when two study factors were present simultaneously. Statistical significance was defined as *p < 0.05, **p < 0.01, ***p < 0.001, and ****p< 0.0001.

Data Availability Statement

The raw data RNA-seq has been deposited in the National Center for Biotechnology Information (https://www.ncbi.nlm.nih.gov/sra/) under the following accession numbers: PRJNA977410 for the RNA-seq data of LLC tumors, PRJNA977566 and PRJNA1129986 for the RNA-seq data of lung tissues with acute RILI, and PRJNA977863 for the single-cell RNA-seq data of lung tissues with chronic RILI. The other data generated in the study are available in the article and its supplementary materials, or from the corresponding author upon reasonable request.

Results

The construction, quantification and validation of JS-201

JS-201 is a fusion protein composed of the Fc C-terminus of toripalimab fused with TGF-βR2 through a (G4S) 4G linker. The short chain of JS-201 consists of two domains, VL from toripalimab and CL as TGF-βR2 amino acid sequences from NCBI gene bank database. The long chain of JS-201 contains five domains: VH, CH1, CH2, CH3, and TGF-βR2. The structural format of JS-201 is illustrated in Figure 1A. SDS-PAGE results showed that a single band over 180 KD was observed without reduction. A long chain between 70 and 100 KD and a short chain between 25 and 35 KD were observed after reduction mediated by DTT (Figure 1B). The results validated the structure of JS-201.

ELISAs were performed to detect the ability of JS-201 to bind to the targets PD-1 and TGF- β 1/2/3 separately and simultaneously. Figure 1C shows that JS-201 has a similar binding capacity to PD-1 targets as anti-PD-1. Figures 1D and 1E suggest that JS-201 binds TGF- β 1 and TGF- β 2 with a similar capacity as TGF- β trap. Figure 1F shows that JS-201 binds TGF- β 3 more weakly than TGF- β trap, while JS-201 has the ability to bind both PD-1 and TGF- β 1/2/3 simultaneously compared to anti PD-1 and TGF- β trap (Figure 1G-I).

JS-201 combined with RT inhibits immune cold tumor growth and prolongs survival

In the single-lesion tumor burden study, three kinds of tumor-bearing models with poor responses to ICB were used to assess the efficacy of combination therapy: the LLC model of lung cancer, the CT26 model of colon cancer and the 4T1 model of breast cancer. Mice were treated as shown in Figure 2A.

In the LLC model, mice in the JS-201 group had a significantly lower tumor burden than those in the anti-PD-1 and NC groups on day 15 post-treatment. In the drug-only group, JS-201 demonstrated stronger antitumor effects and improved survival than NC, anti-PD-1 and TGF- β trap. In the groups that received RT, the combination of JS-201 and RT exhibited a stronger antitumor effect and better survival compared with RT, anti-PD-1+RT and TGF- β trap+RT groups (Figure 2B, 2C).

In the CT26 model, mice in the JS-201 group had a significantly lower tumor

burden than those in the NC and anti-PD-1 groups. The combination of JS-201 and RT had a stronger antitumor growth effect than either JS-201 or RT alone (Figure 2D). The JS-201 group had a significant survival benefit compared to the NC group but did not show a significant survival advantage over the anti-PD-1 group, while there was a significant survival prolongation with the JS-201+RT versus the anti-PD-1 group. Moreover, the JS-201+RT combination significantly prolonged mice survival compared to RT alone, anti-PD-1+RT and TGF-β trap+RT groups (Figure 2E). Similar trends were observed in the 4T1 tumor model (Figure 2F, 2G).

The same tumor models were used to compare JS-201 with the combination of anti-PD-1 and TGF- β trap. In the LLC model, JS-201 had a tendency to reduce tumor burden compared to dual therapy, but the difference was not statistically significant. Similar results were observed between the JS-201+RT and triple therapy groups (Supplementary Figure S1A), while JS-201+RT demonstrated a significant survival advantage over the anti-PD-1+TGF- β trap+RT group (Supplementary Figure S1B). Similar trends were observed in the CT26 and 4T1 tumor models (Supplementary Figure S1C-F).

To further investigate the survival advantage of JS-201+RT over triple therapy, we monitored changes in body weight, liver and kidney function and vital organ damage in both groups of mice for 15 days after treatment. At the observation endpoint, mice in the JS-201+RT group showed significantly less weight loss and less elevated transaminases than those in the anti PD-1+TGF-β trap+RT group (Supplementary Figure S2 A-C) while creatinine levels were not significantly different (Supplementary Figure S2D). HE staining showed that liver tissues were less damaged and structurally disorganised in the JS-201+RT group compared to the triple group of mice (Supplementary Figure S2E).

Combination therapy reversed the immunosuppressive microenvironment

Mice bearing LLC tumors were sacrificed, and the tumors were isolated for pathological staining and IHC after completion of treatment (Figure 3A). The IHC results for CD8 showed a significant increase in tumor-infiltrating cytotoxic

lymphocytes in the JS-201 group compared to the NC, anti-PD-1 and TGF- β trap groups. JS-201+RT further enhanced this effect compared with RT, anti-PD-1+RT and TGF- β trap+RT groups (Supplementary Figure S3A). CD31, a biomarker of vascular endothelium, was used to reflect tumor angiogenesis. The results demonstrated that JS-201 inhibited tumour angiogenesis compared to the NC and anti-PD-1 groups while JS-201+RT resulted in greater antitumor angiogenic activity than RT, anti-PD-1+RT and TGF- β trap+RT groups (Supplementary Figure S3B). Picrosirius red staining indicated that JS-201 significantly reduced fibrosis in the TME compared to NC, anti-PD-1 and TGF- β trap. JS-201+RT exhibited less fibrosis within the TME compared to RT alone and anti PD-1+RT (Supplementary Figure S3C).

LLC tumor tissues from the anti-PD-1, JS-201 and JS-201+RT groups were harvested intact and assayed by transcriptome RNA sequencing to monitor the effects of various treatments. The gene heatmap of the JS-201 compared to the anti-PD-1 groupis shown in Figure 3B and Supplementary Figure S3D, with a total of 1,920 significantly differentially expressed genes (DEGs). We analyzed and counted the top 15 downregulated pathways. GO database enrichment analysis revealed that the JS-201 group had significantly downregulated expression of ECM, cell adhesion, and cell migration compared to the anti-PD-1 group (Figure 3C), which was consistent with the decrease in ECM receptor interactions in KEGG enrichment analysis (Figure 3D). Moreover, JS-201 group significantly down-regulated ECM proteoglycans (Figure S3E) and adenocarcinoma (Figure S3F) expression compared to the anti-PD-1 group.

Significantly expressed genes are displayed in the gene heatmap of the JS-201+RT group relative to the JS-201 group in Figure 3E and Supplementary Figure S3G. We analyzed and counted the top 15 upregulated pathways. GO enrichment analysis suggested that the combination treatment increased gene expression in the ECM, inflammatory response and immune response (Figure 3F). KEGG analysis also showed TNF signaling, cytokine—cytokine receptor interaction and ECM-receptor interaction compared to JS-201 alone (Figure 3G), which was consistent with the Reactome (Supplementary Figure S3H) and DisGeNET (Supplementary Figure S3I) enrichment results. Quantitative PCR was performed using LLC tumors to validate the RNA-seq

results (Figure 3H-Q). These findings suggested that JS-201 attenuated ECM formation and angiogenesis compared to anti-PD-1 and compensated for the negative effects of the ECM induced by RT on the TME. The beneficial effect of combined RT was mainly reflected in the enhancement of the inflammatory response within the tumor.

Combining JS-201 with RT exerts an abscopal effect

A two-focus LLC-luc tumor burden model, as shown in Figure 4A, was established as outlined in a previous study (22) to assess the abscopal effect of combination therapy. Growth curves of primary tumors inoculated in the anterior flank of mice showed a significantly elevated antitumor effect in the combination treatment group compared to the groups with JS-201 and RT alone (Figure 4B). The secondary tumor growth curve showed a significant antitumor effect of JS-201 compared to NC on the distant focus, but there was no significant difference with anti-PD-1. The combination group showed a significant advantage against distant lesions compared to the anti-PD-1 group and was equally superior to the JS-201 and RT alone groups (Figure 4C - 4E. Five mice in each group were selected randomly for in vivo imaging to assess tumor growth (Figure 4F). The results showed that JS-201 reduced the density and fluorescence intensity of primary tumors relative to anti-PD-1 and NC groups, but the combination treatment group showed better antitumor effects in both primary and secondary foci, suggesting that the combination treatment significantly enhanced the abscopal effect.

Combination therapy optimizes immune cell infiltration in primary and secondary tumors

FCM was performed to detect immune cell infiltration, including that of myeloid-derived suppressor cells (MDSCs) (Figure 4G), CD4⁺ and CD8⁺ T cells (Figure 4H), and regulatory T cells (Tregs) (Supplementary Figure S4A) in primary and secondary tumors and spleens of LLC-luc tumor-bearing mice. We utilized CD45+, CD11b+ and Ly6g/Ly6c+ to define MDSCs. MDSCs were significantly reduced after JS-201 treatment compared to NC and anti PD-1, and the enhanced effect of RT on MDSCs was also attenuated in the combination treatment group in primary tumors, secondary

tumors and spleens (Figure 4I-K). Similar trends were also pronounced in Tregs (Supplementary Figure S4B-D).

The ratio of CD8⁺ to CD4⁺ T cells was employed to assess the activity of the cytotoxic response in the TME. The results showed no significant difference between the JS-201 and anti-PD-1 groups, and the combination treatment significantly increased the CD8/CD4 level compared to anti-PD-1, and this level was also significantly higher than that of the RT alone group (Figure 4L). A similar trend was observed in the secondary tumors (Figure 4M) but not in the spleens (Figure 4N). JS-201+RT significantly increased the number of CD4⁺ and CD8⁺ T cells that infiltrated per milligram of tissue compared with other 4 groups (Supplementary Figure S4E-J). The gating strategy is shown in Supplementary Figure S4K-M. These results revealed that the combination of JS-201 and RT enhanced the abscopal effect through elevation of the ratio of CD8⁺/CD4⁺ T cells and diminishment of the number of MDSCs in the primary and secondary tumors.

JS-201 reduces acute/subacute radiation pneumonitis (RP)

A single dose of 16 Gy thoracic radiation was used to generate the acute/subacute RP mouse models, and observation points were set at 1, 2, and 3 months after RT, as shown in Figure 5A. Radiology findings showed that both the RT and anti-PD-1 groups had pronounced fused patchy shadows, solid lesions, and abundant exudate, in contrast to the JS-201 group, which displayed slightly increased bronchovascular shadows, a small amount of exudate and scattered striated foci (Figure 5B). Analysis of CT values used to reflect lung density showed that lung density was lower in the JS-201 group than in the RT and anti-PD-1 groups.at three time points after irradiation (Figure 5C-E).

Left lung tissues of mice were separated for H&E and myeloperoxidase (MPO) staining. The H&E results revealed that the JS-201 group showed less inflammatory infiltration and tissue damage at the observed sites than both the RT and anti-PD-1 groups at 3 time points (Figure 5F). The trend of MPO staining reflecting neutrophil infiltration in terms of temporal variation and severity between groups was consistent with the H&E results (Figure 5G). At the three time points, quantitative analysis showed

that the trend that the JS-201 group showed less MPO infiltration compared to the RT and anti-PD-1 groups remained stable in all subgroups (Figure 5H-J).

JS-201 inhibits the calcium signaling-associated pathway in RP development

Lung tissues from independent acute RILI models were collected for transcriptomic RNA sequencing to investigate the mechanism by which JS-201 attenuated radiation pneumonitis compared to anti-PD-1. Significant DEGs are shown in Figure 5K, with 749 genes significantly down-regulated in the JS-201+RT group compared with the anti-PD-1+RT group (Supplementary Figure S5A). KEGG enrichment results demonstrated that the calcium signaling pathway was inhibited significantly after JS-201 treatment compared to anti-PD-1 treatment (Figure 5L). GO enrichment showed that calcium ion binding and calmodulin binding were significantly decreased in the JS-201 group (Figure 5M). The enrichment analysis of lncRNAs demonstrated similar results (Supplementary Figure S5B-E). The Reactome enrichment analysis of lncRNAs is shown in Supplementary Figure S5F. The simple RT groups were also detected and the DEGs between the simple RT and JS-201+RT groups are shown in Supplementary Figure S6A and B. Anti-PD-1 significantly enhanced the expression of IL-17 pathway (Supplementary Figure S6C) and calcium ion binding (Supplementary Figure S6D) while JS-201 inhibited the ECM-receptor interaction (Supplementary Figure S6E) and calcium ion binding (Supplementary Figure S6F) compared to the RT group.

To further detect key genes in RP progression, we generated Venn diagrams of genes in pathways associated with calcium signaling and inflammation enriched in the GO, KEGG and Reactome databases, as shown in Figure 5N. A total of 5 genes were identified, and the heatmap is shown in Figure 5O. Subsequent validation of differential expression of the 5 genes in the public database GSE174196 for acute RILI suggested that CAMK2A expression was significantly upregulated in the acute RP phase (Figure 5P), while other genes were not expressed or not significantly different in expression (Supplementary Figure S5G, S5H). Lung tissues isolated from acute RP models were used for IHC and Western blot assays to verify the expression of CAMK2A protein among different groups. The IHC results validated the upregulation of CAMK2A in the

anti-PD-1 and RT groups (Figure 5Q, 5R). Western blot results displayed a similar trend and were consistent with the trend of TGF-β1 expression (Figure 5S). The quantitative analysis of band density is shown in Supplementary Figure S5I and J. These results indicated that JS-201 can reduce both CAMK2A and TGF-β1 expression in the lung tissue during RP.

JS-201 mitigates radiation-induced pulmonary fibrosis (RIPF) and prolongs survival

A single dose of 16 Gy thoracic radiation was used to generate the chronic RIPF mouse model with observation points set at 6 months after RT, and JS-201 was administered as shown in Figure 6A. The effects of RIPF on mice were reflected by body weight change curves and percentage survival curves recorded weekly. Statistical analysis showed that the mice in the JS-201+RT group had significantly less weight loss than those in the anti-PD-1+RT group. Although there was no significant difference compared to the RT group, the weight curve showed a rebound trend in the last 6 weeks, contrary to the continuous decline in the RT group (Figure 6B). Furthermore, JS-201+RT significantly prolonged the survival of the mice compared to the RT group (Figure 6C).

Thoracic CT results are displayed in Figure 6D, and analysis of CT values is shown in Figure 6E. These data indicated that the JS-201+RT group had inhibited RIPF compared to the RT and anti-PD-1+RT groups. The pathological staining results are shown in Figure 6F. Statistical analysis showed that the HYP content of the lung tissues in the JS-201+RT group was significantly lower than that in the RT and anti-PD-1+RT groups (Figure 6G). The Ashcroft score (23) employed to interpret the H&E results showed a similar trend (Figure 6H), consistent with Masson (Figure 6I) and picrosirius red staining (Figure 6J).

JS-201 reduces fibroblasts and inhibits the TGF-\(\beta\)1/Smad2 pathway

RIPF mice from the anti-PD-1+RT and JS-201+RT groups were randomly selected for intact isolation of lung tissue for single-cell RNA sequencing to elucidate the potential

mechanism of JS-201 in reducing RIPF compared to anti-PD-1. The TSNE results of 12 kinds of cells collected from the two groups are shown in Figure 6K and UMAP results are shown in Figure 6L. Cellular annotation and analysis of single-cell RNA-seq results were performed using cell markers (Supplementary Table S1). The results of the proportion of the same type of cells between groups are shown in Figure 6M, which demonstrated that JS-201 decrease the proportion of fibroblasts compared to anti PD-1.

Further TSNE analysis of fibroblasts between the two groups was conducted. The original results are shown in Figure 6N. Based on the analysis of genes expressed in clusters (Figure 6O), fibroblasts were further classified into 3 subgroups, which showed that JS-201 reduced all types of fibroblasts (Figure 6P). Moreover, we performed enrichment analysis of intragroup DEGs in order to assess cell function. For the JS-201 group, KEGG enrichment (Figure 6Q) showed no significant difference in the TGF-beta signaling pathway. The TGF-beta signaling pathway was significantly enhanced in fibroblasts in the anti-PD-1 group (Figure 6R).

ELISAs were performed to verify TGF-β1 levels in bronchoalveolar lavage fluid (BALF) and serum of mice, which confirmed that JS-201 reduced TGF-β1 levels compared to the anti-PD-1 and RT groups (Figure 6S, 6T). Western blotting was performed to further verify the expression of the TGF-β/Smad pathway and fibrotic molecules. TGF-β1 increased significantly in the RT and anti-PD-1 groups compared to the NC group, increasing phospho-Smad2 and collagen I/III expression, while both these molecules were distinctly decreased after JS-201 treatment (Figure 6U). The corresponding density analysis of WB bands is shown in Supplementary Figure S7A-F.

JS-201 reduces the formation of neutrophil extracellular traps (NETs)

Single-cell sequencing revealed that the proportion of neutrophils in the JS-201 group was apparently lower than that in the anti-PD-1 group (Figure 6M). In addition to cell proportions, functional differences in neutrophil populations between the two groups were assayed. The heatmap for DEGs between neutrophils is displayed in Supplementary Figure S7G. KEGG enrichment showed a significant decrease in natural

killer cell-mediated cytotoxicity (Figure 7A) in the JS-201 group. GO enrichment showed that the ECM and inflammatory response were significantly decreased in the JS-201+RT group compared to the anti-PD-1+RT group (Figure 7B), suggesting that JS-201 alleviated both inflammatory and fibrotic injury mediated by neutrophils. The original TSNE clustering of neutrophils in the two groups is shown in Figure 7C. A total of 7 genes were analyzed (Supplementary Figure S7H): *Cox6c* and *Cox7c* associated with oxidative stress, Lgals1 associated with ECM, *Gzma* and *Gzmb* associated with cytotoxicity, and *Cybb* and *Cyba* associated with NADPH oxidase. Further clustering results validated that JS-201 significantly reduced neutrophil subpopulations associated with cytotoxicity, ECM and NOX2 compared to anti-PD-1 (Figure 7D), which indicated that NOX2 may play an important role in RIPF development.

To further investigate the mechanism by which neutrophils promoted RIPF, we analyzed total DEGs between the two groups. The expression of genes associated with NETs induced by ROS was significantly increased in the anti-PD-1+RT group, as shown in Figure 7E. Given that Cybb, which encodes NOX2 protein, the precursor of ROS, was highly expressed in the anti-PD-1 group, DHE staining was performed to verify the infiltration of ROS among the groups using frozen BALF and lung tissues (Figure 7F). The results showed that JS-201 significantly decreased ROS in both BALF and lungs compared to the RT and anti-PD-1 groups (Figure 7G, 7H). The expression of a specific marker of NETs, the MPO-DNA complex, was examined using ELISAs in mouse serum and BALF, which showed that the MPO-DNA complex levels were significantly lower in the JS-201 group than in the RT and anti-PD-1 groups (Figure 7I, 7J). Western blotting was performed to further verify the correlation between NETs and RIPF, which showed that JS-201 significantly reduced the expression of NOX2 and CITH3, as well as fibrosis indicators, including α -SMA and COL1A2, compared to the RT and anti-PD-1 groups (Figure 7K). The corresponding density analysis of WB bands is shown in Supplementary Figure S7I-L.

Furthermore, a homologous double-label immunofluorescence assay was performed using CITH3 (green) and MPO (red) to track NETs in lung tissues. DAPI (blue) was used to stain the nucleus. The results showed that NETs, reticular formations

marked by white arrows and expressing both MPO and CITH3, were visible in the thickened alveolar septa, and severe infiltration of neutrophils in the pulmonary interstitium was identified in the RT and anti-PD-1+RT groups compared to the control group. In comparison, no significant release of NETs was observed in the JS-201+RT group (Figure 7L). These findings revealed that JS-201 attenuated RIPF by inhibiting the ratio of neutrophils and NETs formation induced by ROS.

In vivo biosafety evaluation of JS-201

Given the potential adverse effects on the heart of whole thorax irradiation, tumor-bearing mice were selected for the in vivo biosafety assessment of JS-201. The hearts, livers and kidneys of the mice were isolated completely and stained with HE. The myocardial fibers of mice were neatly arranged, the structures of liver lobules and kidney vesicles were clear, and tissues showed no acute damage, such as exudation, congestion, and inflammatory cell infiltration, indicating that in vivo administration of JS-201 did not cause significant damage to major organs (Supplementary Figure S8A).

Serum glutathione aminotransferase (ALT), glutamic oxaloacetic transaminase (AST) and creatinine (Cr) of mice in the NC, anti-PD-1 and JS-201 groups were measured 15 days after the start of treatment. The results showed no significant differences in serum ALT, AST and Cr among these three groups, suggesting that in vivo administration of JS-201 did not affect hepatic and renal function (Supplementary Figure S8B-D).

Together, these results indicate that the combination of JS-201 targeting PD-1 while neutralizing TGF-β1 signaling in a competitive binding manner and single high-dose RT improves antitumor efficacy by optimizing the negative features of the TME while mitigating acute and chronic pulmonary toxicity induced by RT, as shown in Supplementary Figure S8E.

Discussion

Here, we report an immunotherapy–RT combination strategy. We analyzed the effects of JS-201 in combination with RT in terms of antitumor efficacy as well as pulmonary

toxicity and in vivo biosafety, providing a preclinical rationale for the combination of bifunctional antibodies that target both PD-1 and TGF-β signaling with RT.

With the development of immunotherapy, RT, especially stereotactic body radiation therapy (SBRT), is thought to achieve the conversion of immune cold tumors to respond to ICI therapy by improving immunogenic cell death to promote antigen presentation (24, 25), enhancing immune infiltration (26) and releasing cytokines such as TNF- α to promote inflammation within the TME (27), which is concordant with our observation. Since all mice manipulations need to be performed under SPF conditions, the cabinet irradiator was utilized to conduct RT in our research, which is consistent with previous studies (28-30). However, the addition of RT enhances the antitumor immune response while increasing MDSCs (31), TGF-β and PD-1/PD-L1 signaling, leading to both immunosuppression and superimposed toxicity, which is a limitation for combination therapy (32) and is consistent with our findings. Moreover, the stromal component of the TME driven by TGF-β signaling promotes negative features such as tumor angiogenesis, migration, poor immune infiltration and resistance, causing immune evasion (33), which remains a major challenge for the application of ICB and RT in immune-excluded and immune-desert tumors. The TGF-β signaling pathway facilitates the vascular system through endothelial cell remodelling of the TME, thereby promoting tumor angiogenesis and metastasis (34, 35), which is consistent with our findings. Targeting TGF-β signaling alleviates fibrosis in the TME via reduced ECM production, adhesion and deposition, inducing inferior interstitial pressure and thus improving immune cell infiltration (36), which is consistent with our findings.

A previous study revealed that TGF-β inhibition combing RT can promote efficay against NSCLC cells (37). Our results also showed that JS-201 + RT can increase intratumoral inflammation and immune response of LLC. Furthermore, SBRT as a local therapy in combination with systemic ICB can treat unirradiated distant lesions through optimization of immune cell infiltration (38, 39), and the abscopal effect was pronounced as immune evasion was ameliorated by JS-201. Moreover, the combination therapy of JS-201 and RT showed significant survival advantages compared to triple therapy of RT, anti-PD-1 and TGF-β trap on preclinical models due to reduced toxicity

and organ damage, especially liver damage in this research.

A study exploring the bifunctional fusion protein M7824, which targets both PD-L1 and TGF- β signaling, was reported to exert antitumor effects while attenuating RIPF (18), which is consistent with our findings. Given the disruption of oncologic treatment, the poor prognostic impact and even lethality for patients caused by acute radiation pneumonitis, we also conducted experiments, analysis and validation of the effects of JS-201 on RP. RP is a noninfectious inflammation mediated by radiation-generated ROS that primarily injures vascular endothelial and alveolar epithelial cells, provoking aggravated capillary permeability, inflammatory cell infiltration and pulmonary edema (40, 41). The calcium signaling pathway and downstream binding proteins play an important role in promoting vascular permeability induced by inflammatory mediators (42) and regulating the activity of transient receptor potential (TRP) channels (43). Furthermore, previous studies revealed that TGF- β stimulation could increase calcium signaling (44, 45) and that CAMK2 played a key role in acute injury induced by ROS (46-49), which is consistent with our results.

Prolonged inflammatory infiltration and persistent ROS injury activate TGF-β signaling, which induces fibroblast proliferation, myofibroblast differentiation, and ECM formation, ultimately leading to fibrogenesis (50). A series of studies have shown that fibroblast proliferation can be regulated by the TGF-β signaling pathway and promote collagen deposition (51-54), consistent with our single-cell sequencing and Western blot results. Because RILI is a continuous dynamic process, the transitional role of neutrophils as the first inflammatory cell population to infiltrate the injury site (55) deserves more attention. The prolonged presence of neutrophils leads to an increase in NETs (56), which further exacerbates inflammation while leading to fibrosis, and this process can be stimulated by ROS (57). Furthermore, many studies have revealed that NETs can promote ECM and organ fibrosis (58-61), which is consistent with our results. The role of NETs in chronic lung disease has been reported, but no studies have identified the effect of NETs in RILI. Our results demonstrated that neutrophils, which have a connective role in inflammation-fibrosis, released NETs to promote RIPF in response to ROS stimulation and that JS-201 attenuated this process

by downregulating NOX2 through inhibition of TGF- β signaling, suggesting that NETs may be a potential target for RILI therapy.

Single agent M7824, which targets TGF-β signaling and PD-L1, failed in both a phase II clinical trial for advanced biliary tract cancer and a phase III trial for non-small cell lung cancer (NSCLC), despite achieving significant antitumor effects connected with RT in preclinical research. Paradoxically, immunoradiotherapy achieved significant efficacy in early-stage NSCLC (62) and potential efficacy in metastatic NSCLC patients with low PD-L1 expression. Notably, this Phase I/II clinical study (63) found that SBRT increased the objective remission rate of out-field lesions compared to traditional RT when combined with pembrolizumab (38% VS 10%). Furthermore, a previous overview summarized that single fraction stereotactic ablative body radiotherapy (SABR) not only induces DNA damage, but also vascular damage and immune response, which can induce indirect tumor cell death (64). Therefore, we also chose single fraction instead of traditional RT in this research. These results indicated that local RT may play an essential role in both early and advanced cancers with poor immune features. Our study also confirmed that the addition of RT enhanced the inflammatory response within the tumor and increased CD8⁺ T-cell infiltration. Given the failure of M7824 in clinical trials, the bifunctional antibody JS-201 we used with different targets may be valuable for clinical application, and a phase I clinical trial of humanized JS-201 in patients with advanced malignant tumors is currently underway (NCT04956926). Moreover, our study provides theoretical support for subsequent attempts to combine dual-target immunotherapy with JS-201 with RT in the clinic.

However, the following limitations exist in our study. Due to the lack of a public database on RILI in humans, we lack clinical validation of the effects on the calcium signaling pathway and CAMK2 during acute/subacute RILI, which we intend to address through retrospective clinical analysis in the future. Moreover, there may be an increase in abdominal exposure due to our use of cabinet irradiators and lead plate masking for irradiation. Finally, the efficacy of JS-201 in treating RILI has not been clinically proven; thus, we are interested in conducting clinical trials of JS-201 in combination with RT in advanced thoracic tumors in the future.

In summary, JS-201 mitigates the immunosuppressive features of the TME driven by TGF- β signaling compared to anti-PD-1, and the combination with RT increases the inflammatory response and immune infiltration while compensating for the double-sided nature of RT within the TME. Targeting TGF- β signaling attenuates both RP, by inhibiting the calcium signaling pathway, and RIPF, by reducing fibroblast proliferation and NET release stimulated by ROS, suggesting that the combination of JS-201 and RT enhances antitumor effects while mitigating acute and chronic RILI.

Acknowledgements

We thank Experimental Medicine Center of Tongji Hospital, Tongji Medical College, Huazhong University of Science and Technology for assistance of flow cytometry. We thank Medical Subcenter of HUST Analytical & Testing Center for operation guidance of micro-CT. We thank the analytical data provided by the TCGA, GEO, DisGeNET and Reactome databases.

Ethics

All animal experiments in this study were approved by the Ethics Committee of Huazhong University of Science and Technology (Hubei, China). The IACUC number is 3224.

References

- 1. Sung H, Ferlay J, Siegel RL, et al. Global Cancer Statistics 2020: GLOBOCAN Estimates of Incidence and Mortality Worldwide for 36 Cancers in 185 Countries. CA Cancer J Clin. 2021;71(3):209-249.
- 2. Dillon MT, Bergerhoff KF, Pedersen M, et al. ATR Inhibition Potentiates the Radiation-induced Inflammatory Tumor Microenvironment. Clin Cancer Res. 2019;25(11):3392-3403.
- 3. Bian Z, Shi L, Kidder K, Zen K, Garnett-Benson C, Liu Y. Intratumoral SIRPα-deficient macrophages activate tumor antigen-specific cytotoxic T cells under radiotherapy. Nat Commun. 2021;12(1):3229.

- 4. Ahmed A, Tait SWG. Targeting immunogenic cell death in cancer. Mol Oncol. 2020;14(12):2994-3006.
- 5. Han C, Liu Z, Zhang Y, et al. Tumor cells suppress radiation-induced immunity by hijacking caspase 9 signaling. Nat Immunol. 2020;21(5):546-554.
- 6. Hegde PS, Chen DS. Top 10 Challenges in Cancer Immunotherapy. Immunity. 2020;52(1):17-35.
- 7. Haslam A, Prasad V. Estimation of the Percentage of US Patients With Cancer Who Are Eligible for and Respond to Checkpoint Inhibitor Immunotherapy Drugs. JAMA Netw Open. 2019;2(5):e192535.
- 8. Wong KCW, Johnson D, Hui EP, Lam RCT, Ma BBY, Chan ATC. Opportunities and challenges in combining immunotherapy and radiotherapy in head and neck cancers. Cancer Treat Rev. 2022;105:102361.
- 9. Arina A, Gutiontov SI, Weichselbaum RR. Radiotherapy and Immunotherapy for Cancer: From "Systemic" to "Multisite". Clin Cancer Res. 2020;26(12):2777-2782.
- 10. Mondini M, Levy A, Meziani L, Milliat F, Deutsch E. Radiotherapy-immunotherapy combinations perspectives and challenges. Mol Oncol. 2020;14(7):1529-1537.
- 11. Anscher MS, Arora S, Weinstock C, et al. Association of Radiation Therapy With Risk of Adverse Events in Patients Receiving Immunotherapy: A Pooled Analysis of Trials in the US Food and Drug Administration Database. JAMA Oncol. 2022;8(2):232-240.
- 12. Hui R, Özgüroğlu M, Villegas A, et al. Patient-reported outcomes with durvalumab after chemoradiotherapy in stage III, unresectable non-small-cell lung cancer (PACIFIC): a randomised, controlled, phase 3 study. Lancet Oncol. 2019;20(12): 1670-1680.
- 13.Li B, Jiang C, Pang L, et al. Toxicity Profile of Combining PD-1/PD-L1 Inhibitors and Thoracic Radiotherapy in Non-Small Cell Lung Cancer: A Systematic Review. Front Immunol. 2021;12:627197.
- 14.David CJ, Massagué J. Contextual determinants of TGFβ action in development, immunity and cancer. Nat Rev Mol Cell Biol. 2018;19(7):419-435.
- 15. Tauriello DVF, Sancho E, Batlle E. Overcoming TGFβ-mediated immune evasion

- in cancer. Nat Rev Cancer. 2022;22(1):25-44.
- 16. Käsmann L, Dietrich A, Staab-Weijnitz CA, et al. Radiation-induced lung toxicity cellular and molecular mechanisms of pathogenesis, management, and literature review. Radiat Oncol. 2020;15(1):214.
- 17. Jie X, Fong WP, Zhou R, et al. USP9X-mediated KDM4C deubiquitination promotes lung cancer radioresistance by epigenetically inducing TGF-β2 transcription. Cell Death Differ. 2021;28(7):2095-2111.
- 18.Lan Y, Moustafa M, Knoll M, et al. Simultaneous targeting of TGF-β/PD-L1 synergizes with radiotherapy by reprogramming the tumor microenvironment to overcome immune evasion. Cancer Cell. 2021;39(10):1388-1403.e10.
- 19.Cho BC, Lee JS, Wu YL, et al. Bintrafusp Alfa Versus Pembrolizumab in Patients With Treatment-Naive, Programmed Death-Ligand 1-High Advanced NSCLC: A Randomized, Open-Label, Phase 3 Trial. J Thorac Oncol. 2023; S1556-0864(23)00738-4.
- 20. Yoo C, Javle MM, Verdaguer Mata H, et al. Phase 2 trial of bintrafusp alfa as second-line therapy for patients with locally advanced/metastatic biliary tract cancers. Hepatology. 2023;78(3):758-770.
- 21. Hwang WL, Pike LRG, Royce TJ, Mahal BA, Loeffler JS. Safety of combining radiotherapy with immune-checkpoint inhibition. Nat Rev Clin Oncol. 2018;15(8):477-494.
- 22. Ji D, Song C, Li Y, et al. Combination of radiotherapy and suppression of Tregs enhances abscopal antitumour effect and inhibits metastasis in rectal cancer. J Immunother Cancer. 2020;8(2):e000826.
- 23. Ashcroft T, Simpson JM, Timbrell V. Simple method of estimating severity of pulmonary fibrosis on a numerical scale. J Clin Pathol. 1988;41(4):467-470.
- 24. Hsieh RC, Krishnan S, Wu RC, et al. ATR-mediated CD47 and PD-L1 upregulation restricts radiotherapy-induced immune priming and abscopal responses in colorectal cancer. Sci Immunol. 2022;7(72):eabl9330.
- 25.Guan X, Sun L, Shen Y, et al. Nanoparticle-enhanced radiotherapy synergizes with PD-L1 blockade to limit postsurgical cancer recurrence and metastasis. Nat Commun.

- 2022;13(1):2834.
- 26. Formenti SC, Rudqvist NP, Golden E, et al. Radiotherapy induces responses of lung cancer to CTLA-4 blockade. Nat Med. 2018;24(12):1845-1851.
- 27.Rao E, Hou Y, Huang X, et al. All-trans retinoic acid overcomes solid tumor radioresistance by inducing inflammatory macrophages. Sci Immunol. 2021;6(60):eaba8426.
- 28.Boria AJ, Perez-Torres CJ. Minimal difference between fractionated and single-fraction exposure in a murine model of radiation necrosis. Radiat Oncol. 2019;14(1):144.
- 29.To NH, Pilon C, Moatti A, et al. Effect of lethal total body irradiation on bone marrow chimerism, acute graft-versus-host disease, and tumor engraftment in mouse models: impact of different radiation techniques using low- and high-energy X-rays. Strahlenther Onkol. 2023;199(12):1242-1254.
- 30.Liu C, Wang X, Qin W, et al. Combining radiation and the ATR inhibitor berzosertib activates STING signaling and enhances immunotherapy via inhibiting SHP1 function in colorectal cancer. Cancer Commun (Lond). 2023;43(4):435-454.
- 31.Kho VM, Mekers VE, Span PN, Bussink J, Adema GJ. Radiotherapy and cGAS/STING signaling: Impact on MDSCs in the tumor microenvironment. Cell Immunol. 2021;362:104298.
- 32. Mondini M, Levy A, Meziani L, Milliat F, Deutsch E. Radiotherapy-immunotherapy combinations perspectives and challenges. Mol Oncol. 2020;14(7):1529-1537.
- 33. Morad G, Helmink BA, Sharma P, Wargo JA. Hallmarks of response, resistance, and toxicity to immune checkpoint blockade. Cell. 2021;184(21):5309-5337.
- 34. Watabe T, Takahashi K, Pietras K, Yoshimatsu Y. Roles of TGF-β signals in tumor microenvironment via regulation of the formation and plasticity of vascular system. Semin Cancer Biol. 2023;92:130-138.
- 35.van Loon K, Yemelyanenko-Lyalenko J, Margadant C, Griffioen AW, Huijbers EJM. Role of fibrillin-2 in the control of TGF-β activation in tumor angiogenesis and connective tissue disorders. Biochim Biophys Acta Rev Cancer. 2020;1873(2):188354. 36.Perez-Penco M, Weis-Banke SE, Schina A, et al. TGFβ-derived immune modulatory

- vaccine: targeting the immunosuppressive and fibrotic tumor microenvironment in a murine model of pancreatic cancer. J Immunother Cancer. 2022;10(12):e005491.
- 37.Du S, Bouquet S, Lo CH, et al. Attenuation of the DNA damage response by transforming growth factor-beta inhibitors enhances radiation sensitivity of non-small-cell lung cancer cells in vitro and in vivo. Int J Radiat Oncol Biol Phys. 2015;91(1):91-99.
- 38. Nishiga Y, Drainas AP, Baron M, et al. Radiotherapy in combination with CD47 blockade elicits a macrophage-mediated abscopal effect. Nat Cancer. 2022;3(11):1351-1366.
- 39. Ashrafizadeh M, Farhood B, Eleojo Musa A, Taeb S, Rezaeyan A, Najafi M. Abscopal effect in radioimmunotherapy. Int Immunopharmacol. 2020;85:106663.
- 40.Khodamoradi E, Hoseini-Ghahfarokhi M, Amini P, et al. Targets for protection and mitigation of radiation injury. Cell Mol Life Sci. 2020;77(16):3129-3159.
- 41. Hanania AN, Mainwaring W, Ghebre YT, Hanania NA, Ludwig M. Radiation-Induced Lung Injury: Assessment and Management. Chest. 2019;156(1):150-162.
- 42. Dalal PJ, Muller WA, Sullivan DP. Endothelial Cell Calcium Signaling during Barrier Function and Inflammation. Am J Pathol. 2020;190(3):535-542.
- 43. Zhong T, Zhang W, Guo H, et al. The regulatory and modulatory roles of TRP family channels in malignant tumors and relevant therapeutic strategies. Acta Pharm Sin B. 2022;12(4):1761-1780.
- 44. Mukherjee S, Sheng W, Michkov A, et al. Prostaglandin E2 inhibits profibrotic function of human pulmonary fibroblasts by disrupting Ca2+ signaling. Am J Physiol Lung Cell Mol Physiol. 2019;316(5):L810-L821.
- 45. Joseph JV, Magaut CR, Storevik S, et al. TGF-β promotes microtube formation in glioblastoma through thrombospondin 1. Neuro Oncol. 2022;24(4):541-553.
- 46. Jiang J, Huang K, Xu S, Garcia JGN, Wang C, Cai H. Targeting NOX4 alleviates sepsis-induced acute lung injury via attenuation of redox-sensitive activation of CaMKII/ERK1/2/MLCK and endothelial cell barrier dysfunction. Redox Biol. 2020;36:101638.
- 47.Zhu Q, Hao L, Shen Q, et al. CaMK II Inhibition Attenuates ROS Dependent

- Necroptosis in Acinar Cells and Protects against Acute Pancreatitis in Mice. Oxid Med Cell Longev. 2021;2021:4187398.
- 48. Suetomi T, Willeford A, Brand CS, et al. Inflammation and NLRP3 Inflammasome Activation Initiated in Response to Pressure Overload by Ca2+/Calmodulin-Dependent Protein Kinase II δ Signaling in Cardiomyocytes Are Essential for Adverse Cardiac Remodelling. Circulation. 2018;138(22):2530-2544.
- 49.Qi Y, Xu H, Li X, et al. Silica nanoparticles induce cardiac injury and dysfunction via ROS/Ca2+/CaMKII signaling. Sci Total Environ. 2022;837:155733.
- 50.Zhao M, Wang L, Wang M, et al. Targeting fibrosis, mechanisms and cilinical trials. Signal Transduct Target Ther. 2022;7(1):206.
- 51.Cheng F, Shen Y, Mohanasundaram P, et al. Vimentin coordinates fibroblast proliferation and keratinocyte differentiation in wound healing via TGF-β-Slug signaling. Proc Natl Acad Sci U S A. 2016;113(30):E4320-E4327.
- 52. Chung JY, Chan MK, Li JS, et al. TGF-β Signaling: From Tissue Fibrosis to Tumor Microenvironment. Int J Mol Sci. 2021;22(14):7575.
- 53. Wang XM, Liu XM, Wang Y, Chen ZY. Activating transcription factor 3 (ATF3) regulates cell growth, apoptosis, invasion and collagen synthesis in keloid fibroblast through transforming growth factor beta (TGF-beta)/SMAD signaling pathway. Bioengineered. 2021;12(1):117-126.
- 54.Zerr P, Palumbo-Zerr K, Huang J, et al. Sirt1 regulates canonical TGF-β signalling to control fibroblast activation and tissue fibrosis. Ann Rheum Dis. 2016;75(1):226-233.
- 55. Straub JM, New J, Hamilton CD, Lominska C, Shnayder Y, Thomas SM. Radiation-induced fibrosis: mechanisms and implications for therapy. J Cancer Res Clin Oncol. 2015;141(11):1985-1994.
- 56. Gray RD, Hardisty G, Regan KH, et al. Delayed neutrophil apoptosis enhances NET formation in cystic fibrosis. Thorax. 2018;73(2):134-144.
- 57.Lood C, Blanco LP, Purmalek MM, et al. Neutrophil extracellular traps enriched in oxidized mitochondrial DNA are interferogenic and contribute to lupus-like disease. Nat Med. 2016;22(2):146-153.

- 58. Wang Y, Li Y, Chen Z, et al. GSDMD-dependent neutrophil extracellular traps promote macrophage-to-myofibroblast transition and renal fibrosis in obstructive nephropathy. Cell Death Dis. 2022;13(8):693.
- 59. Suzuki M, Ikari J, Anazawa R, et al. PAD4 Deficiency Improves Bleomycin-induced Neutrophil Extracellular Traps and Fibrosis in Mouse Lung. Am J Respir Cell Mol Biol. 2020;63(6):806-818.
- 60. Sharma S, Hofbauer TM, Ondracek AS, et al. Neutrophil extracellular traps promote fibrous vascular occlusions in chronic thrombosis. Blood. 2021;137(8):1104-1116.
- 61.Zhang XL, Wang TY, Chen Z, et al. HMGB1-Promoted Neutrophil Extracellular Traps Contribute to Cardiac Diastolic Dysfunction in Mice. J Am Heart Assoc. 2022;11(4):e023800.
- 62. Altorki NK, McGraw TE, Borczuk AC, et al. Neoadjuvant durvalumab with or without stereotactic body radiotherapy in patients with early-stage non-small cell lung cancer: a single-centre, randomized phase 2 trial. Lancet Oncol. 2021;22(6):824-835.
- 63. Welsh J, Menon H, Chen D, et al. Pembrolizumab with or without radiation therapy for metastatic non-small cell lung cancer: a randomized phase I/II trial. J Immunother Cancer. 2020;8(2):e001001.
- 64. Tjong MC, Louie AV, Singh AK, et al. Single-Fraction Stereotactic Ablative Body Radiotherapy to the Lung The Knockout Punch. Clin Oncol (R Coll Radiol). 2022;34(5):e183-e194.

Figure legends

Figure 1. Construction, quantification and validation of JS-201. (A) The structure of JS-201. (B) SDS-PAGE results of intact and reduced JS-201. (C) The ability of JS-201 to bind PD-1, (D) TGF- β 1, (E) TGF- β 2 and (F) TGF- β 3 separately. (G) The ability of JS-201 to bind TGF- β 1+PD-1, (H) TGF- β 2+PD-1 and (I) TGF- β 3+PD-1 simultaneously.

Figure 2. JS-201 combined with RT inhibited immune cold tumor growth and prolonged survival. (A) The construction and treatment of tumor-bearing mice. (B) Tumor growth curves of LLC models. N=9; mean \pm SEM; Two-way ANOVA analysis. (C) Survival curves of LLC models. N=9; Kaplan-Meier curves with Cox tests. (D) Tumor growth curves of CT26 models. N=9; mean \pm SEM; Two-way ANOVA analysis. (E) Survival curves of CT26 models. Kaplan-Meier curves with Cox tests. (F) Tumor growth curves of 4T1 models. N=7; mean \pm SEM; Two-way ANOVA analysis. (G) Survival curves of 4T1 models. N=7; mean \pm SEM; Kaplan-Meier curves with Cox tests. *, p < 0.05; ***, p < 0.01; ****, p < 0.001; ****, p < 0.001; ****, p < 0.0001; ns, no significance.

Figure 3. Combination therapy reversed the immunosuppressive microenvironment. (A) CD8, CD31 and picrosirius red staining of LLC tumors. N=3. (B) Heatmap of significant DEGs of LLC tumors in the JS-201 and anti-PD-1 groups. N=3. (C) GO and (D) KEGG enrichment of DEGs downregulated by JS-201 compared to anti-PD-1. (E) Heatmap of significant DEGs of LLC tumors in the JS-201 and combination therapy groups. (F) GO and (G) KEGG enrichment of DEGs upregulated by combination therapy compared to JS-201. (H-Q) The results of qPCR using LLC tumors. N=3; mean \pm SD; One-way ANOVA analysis. The white and black scale bar is 100 μ m. DEGs, differentially expressed genes. *, p < 0.05; **, p < 0.01; ***, p < 0.001; ****, p < 0.0001; *****, p < 0.0001; ******, p < 0.0001; *******, p < 0.0001; *******, p < 0.0001; ******, p < 0.0001; *******, p < 0.0001; ******, p

Figure 4. Combination therapy exerted a significant abscopal effect by enhancing immune infiltration. (A) Construction and treatment of the dual LLC-luc tumor-bearing

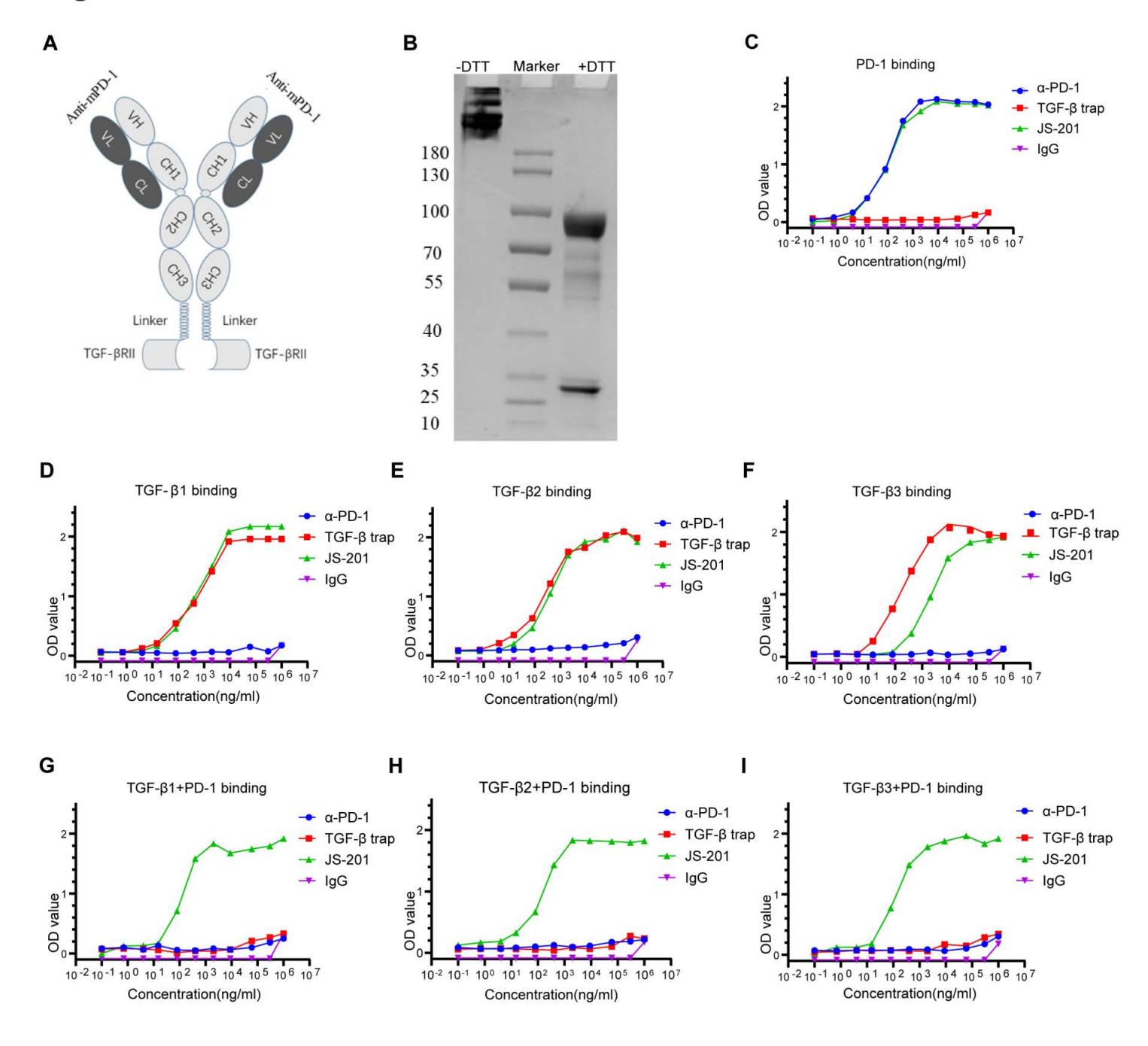
model. (B) Primary and (C) secondary tumor growth curves. N=10; mean \pm SEM; Twoway ANOVA analysis. (D) In vivo fluorescence imaging of mouse models. N=5. (E) Images of isolated primary tumors. N=5. (F) Images of isolated secondary tumors. N=5. (G) MDSCs in primary tumors, secondary tumors and spleens. (H-J) Analysis of the cell amount per milligram of MDSCs. (K) CD8+ and CD4+ T cells in primary tumors, secondary tumors and spleens. (L-N) Analysis of the ratio of CD8/CD4. N=3; mean \pm SD; One-way ANOVA analysis. The black circle represents tumor regression. *, p < 0.05; ***, p < 0.01; ****, p < 0.001; *****, p < 0.0001; ns, no significance.

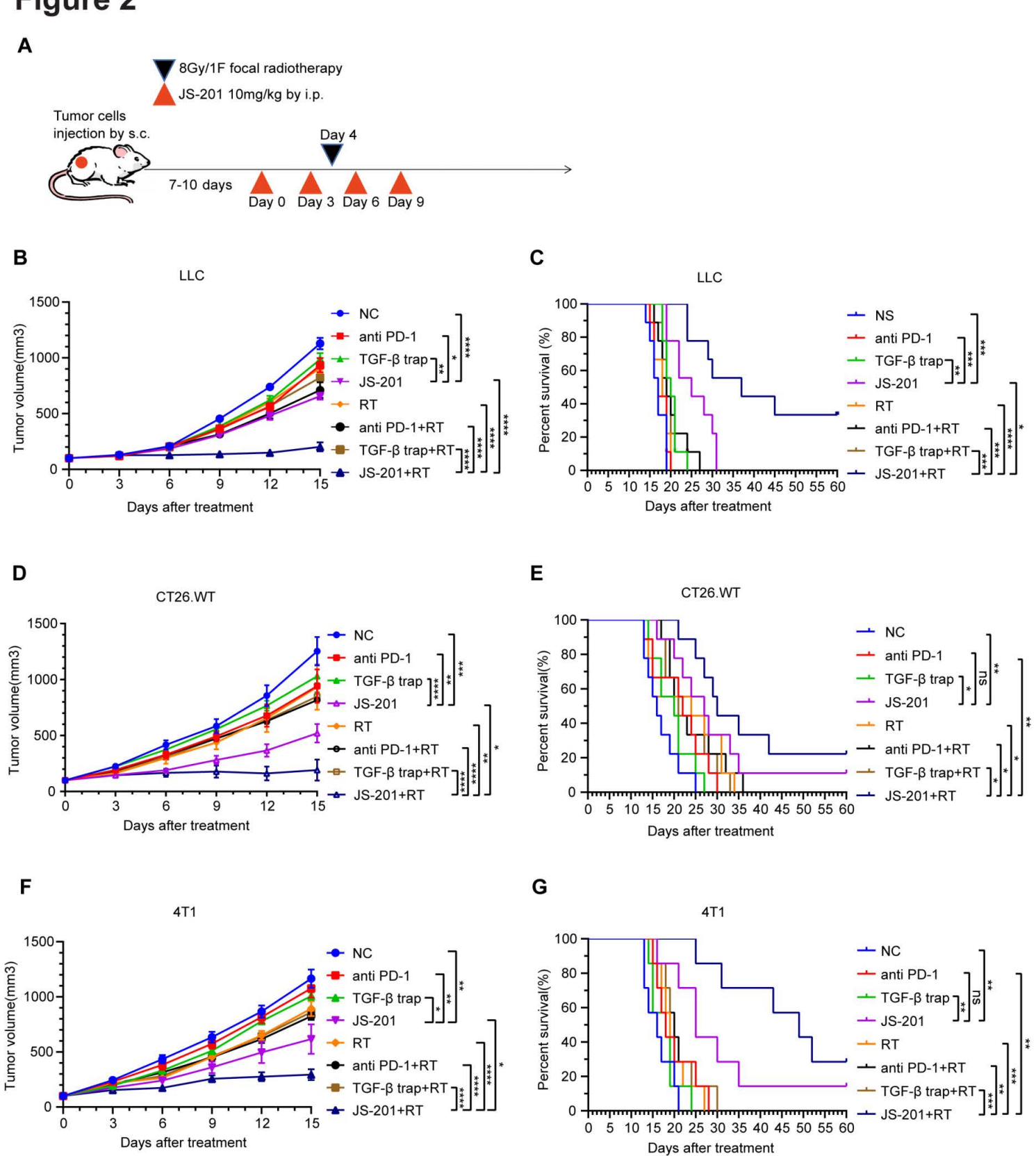
Figure 5. JS-201 reduced RP through inhibition of the calcium signaling pathway. (A) Construction, treatment and observation of RP models. (B) Pulmonary CT images of mice 1, 2 and 3 months after RT. (C-E) Analysis of lung density at three time points. (F) HE and (G) MPO staining of lung tissues. (H-J) Analysis of the positive area of MPO. N=3; mean \pm SD; One-way ANOVA analysis. (K) Heatmap of significant DEGs of lungs with RP in the JS-201 and anti-PD-1 groups. N=3. (L) KEGG and (M) GO enrichment results of DEGs downregulated by JS-201 compared to anti-PD-1. (N) Venn diagrams of genes in the top pathways in GO, KEGG and Reactome enrichment. (O) Heatmap of genes intersecting in the Venn diagram. (P) The expression of CAMK2A in the GSE 174196 dataset. (Q) IHC images of CAMK2A in lung tissues 1 month after RT. (R) Analysis of the CAMK2A-positive area. N=3; mean \pm SD; One-way ANOVA analysis. (S) Western blot images of CAMK2A and TGF- β 1 in lungs. The black scale bar is 100 μ m. The red scale bar is 200 μ m. RP, radiation pneumonitis; RT, radiotherapy; *, p < 0.05; ***, p < 0.01; ****, p < 0.001; *****, p < 0.0001.

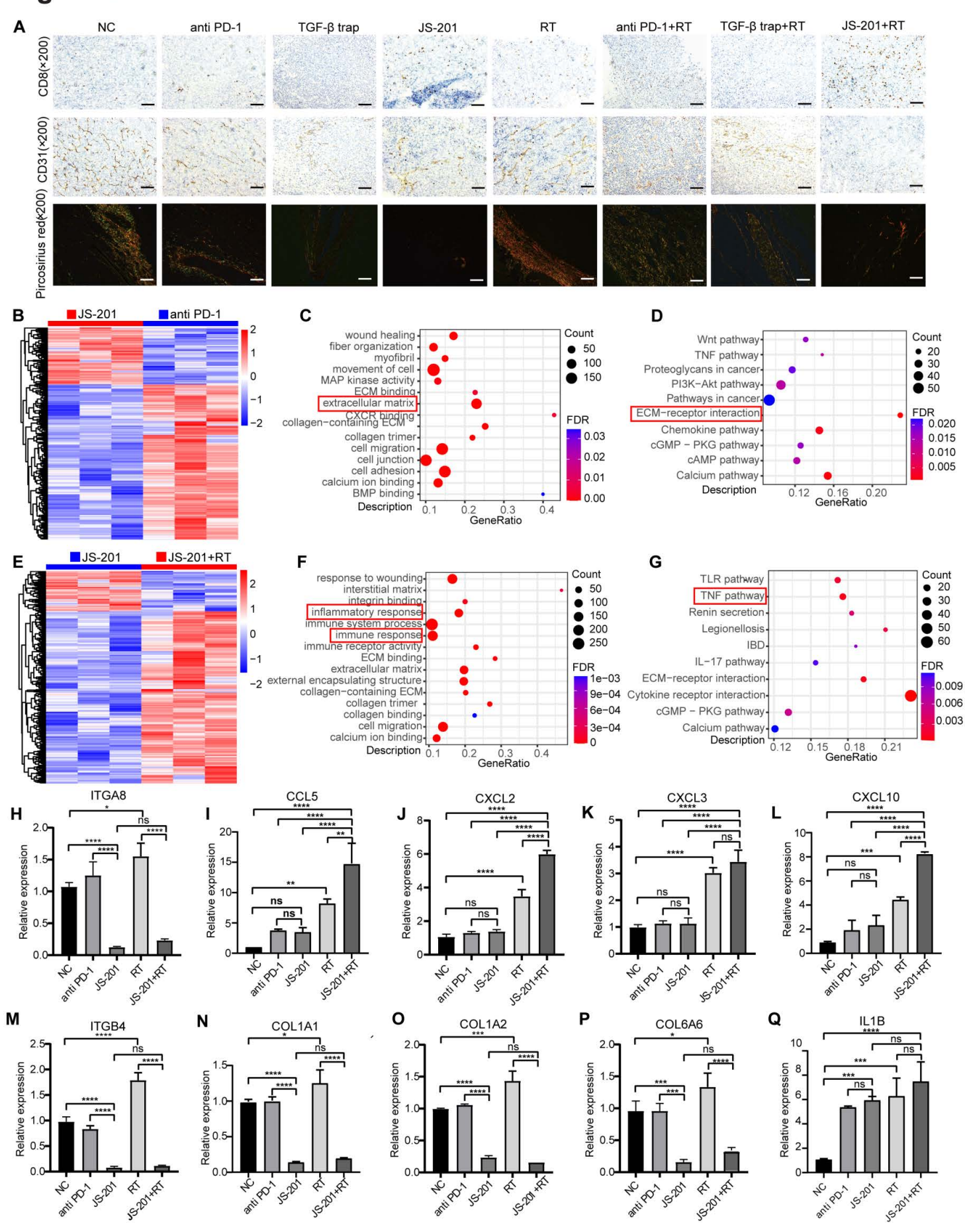
Figure 6. JS-201 mitigated RIPF and prolonged survival. (A) Construction and treatment of RIPF models. (B) Body weight change curves of mice. N=15; mean ± SEM; Two-way mixed-effect model ANOVA analysis. (C) Survival curves of RIPF models. N=15; mean ± SEM; Kaplan-Meier curves with Cox tests. (D) Thoracic CT images of RIPF models 6 months after RT. (E) The density of lungs is presented using CT values. N=5; mean ± SD; One-way ANOVA analysis. (F) HE, Masson and

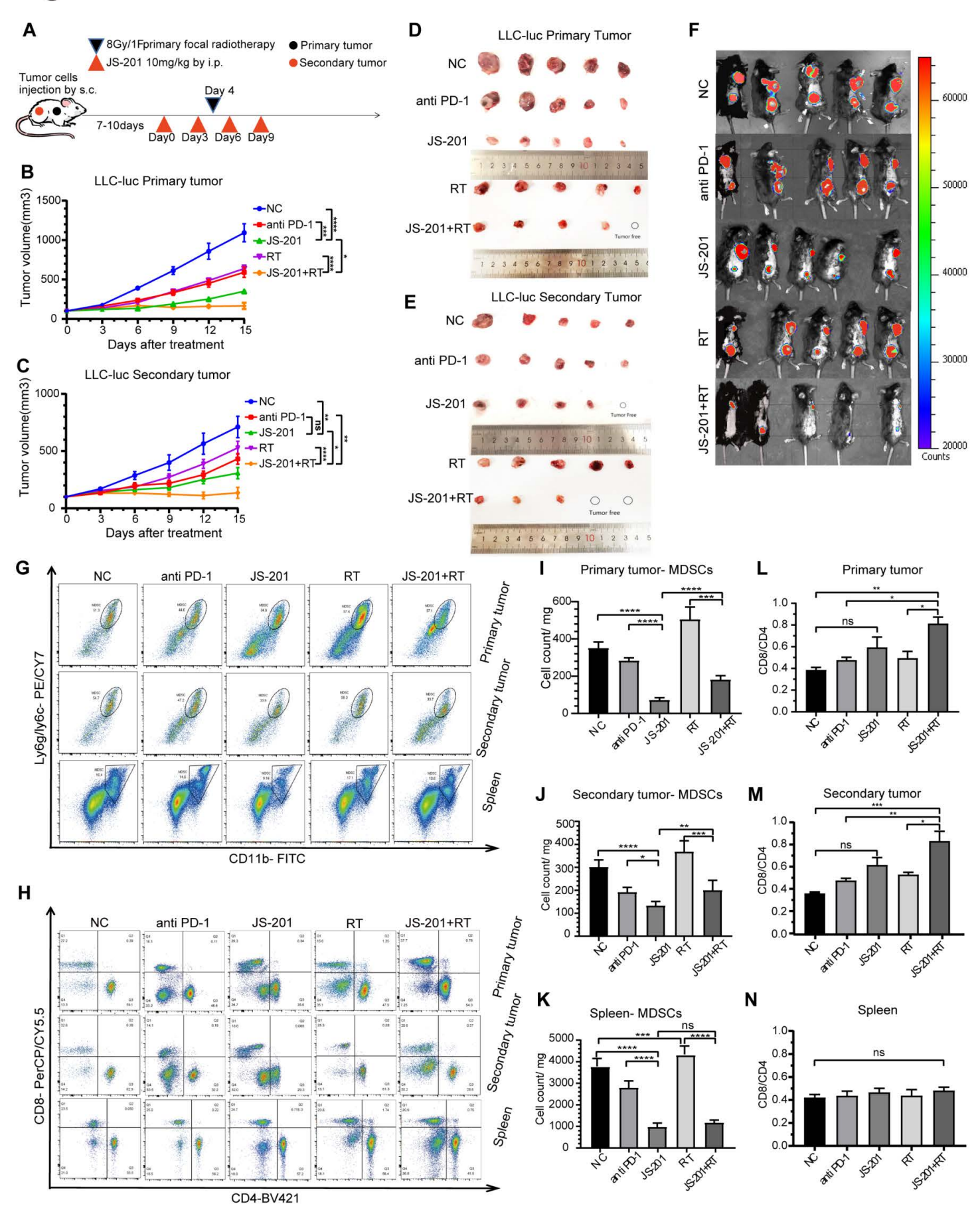
picrosirius red staining of lungs. (G) HYP content of lungs. (H) Analysis of Ashcroft scores. (I) Analysis of the positive percentage of Masson and (J) picrosirius red staining. N=3; mean \pm SD; One-way ANOVA analysis. (K) TSNE and (L) UMAP results of single-cell RNA-seq of lung tissues in the JS-201 and anti-PD-1 groups at 6 months after radiotherapy. (M) Comparison of the same cell types between the JS-201 and anti-PD-1 groups. (N) Original TSNE clustering analysis of fibroblasts. (O) Results of gene expression among 7 clusters. (P) Further TSNE clustering analysis of fibroblasts based on gene expression. (Q) KEGG enrichment of DEGs of fibroblasts in the JS-201 group. (R) KEGG enrichment of DEGs of fibroblasts in the anti-PD-1 group. (S) TGF-β1 levels in the serum of each group. (T) TGF-β1 levels in BALF of each group. N=4; mean \pm SD; One-way ANOVA analysis. (U) Western blot images of COL3A1, COL1A2, Smad2, pSmad2 and TGF-β1 in lung tissues. The black and white scale bar is 100 μm. The red scale bar is 200 μm. RIPF, radiation-induced pulmonary fibrosis. *, p < 0.05; **, p < 0.01; ***, p < 0.001; ****, p < 0.00101.

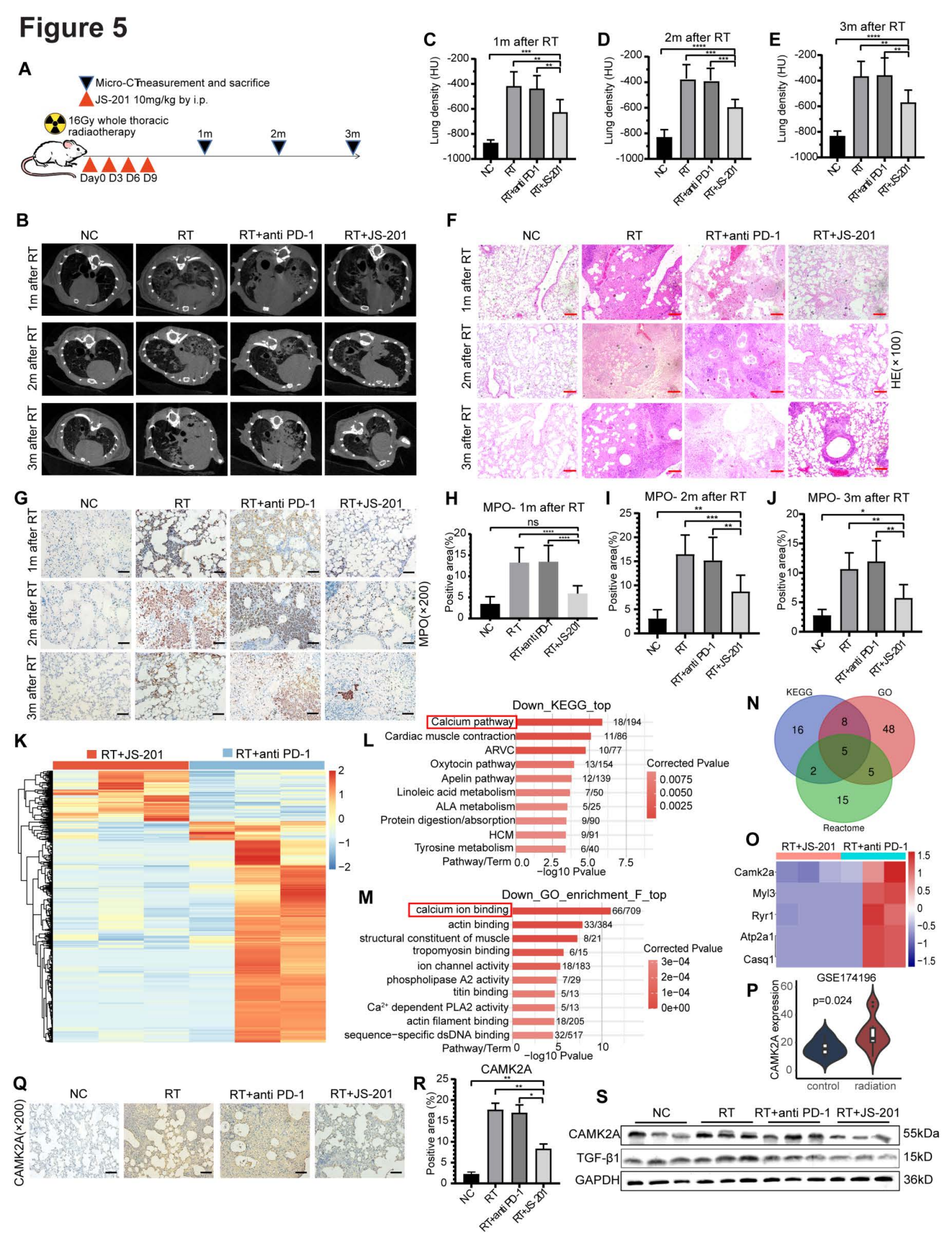
Figure 7. JS-201 reduced the ratio of neutrophils and NET formation induced by ROS. (A) KEGG and (B) GO enrichment of significant DEGs of neutrophils between the JS-201 and anti-PD-1 groups. (C) Original TSNE clustering analysis of neutrophils. (D) Further TSNE clustering analysis of neutrophils based on 7 characteristic genes. (E) Heatmap of target DEGs between the JS-201 and anti-PD-1 groups. (F) DHE staining of lung tissues and BALF. (G) The percentage of positive area of lungs and (H) BALF. N=3; mean \pm SD; One-way ANOVA analysis. (I) MPO-DNA levels in mouse serum. (J) MPO-DNA levels in mouse BALF. N=4; mean \pm SD; One-way ANOVA analysis. (K) Western blot images of COL1A2, NOX2, α -SMA and CITH3. (L) Double-labelled IF images of lung tissues. Red refers to MPO staining. Green refers to CITH3 staining. Blue refers to DAPI staining. The white arrow indicates NETs. The orange scale bar is 50 μ m. BALF, bronchoalveolar lavage fluid; CITH3, citrulline histone H3; DHE, dihydroethidium; MPO, myeloperoxidase; NETs, neutrophil extracellular traps; ROS, reactive oxygen species; *, p < 0.05; ***, p < 0.01; ****, p < 0.001; *****, p < 0.0001.

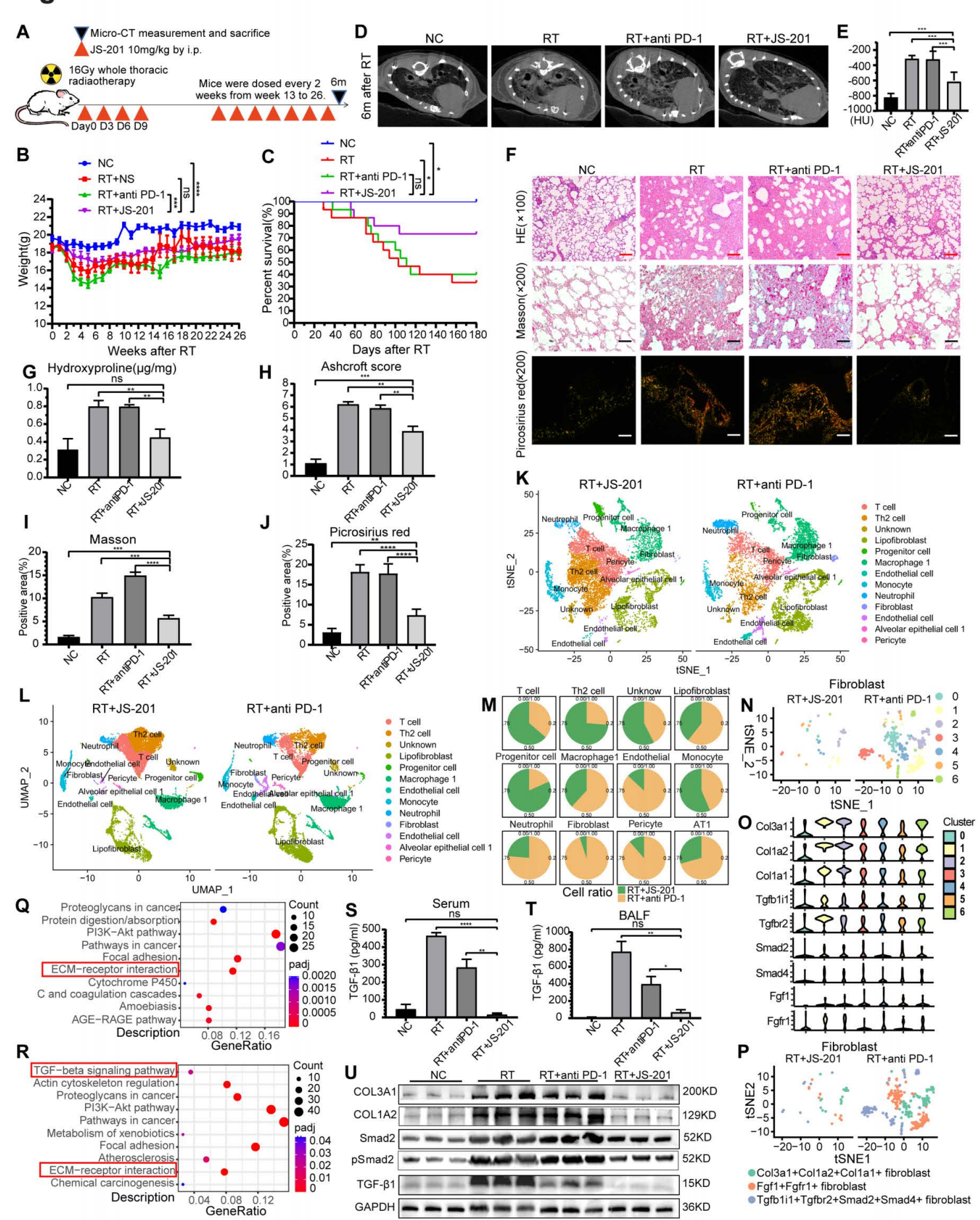


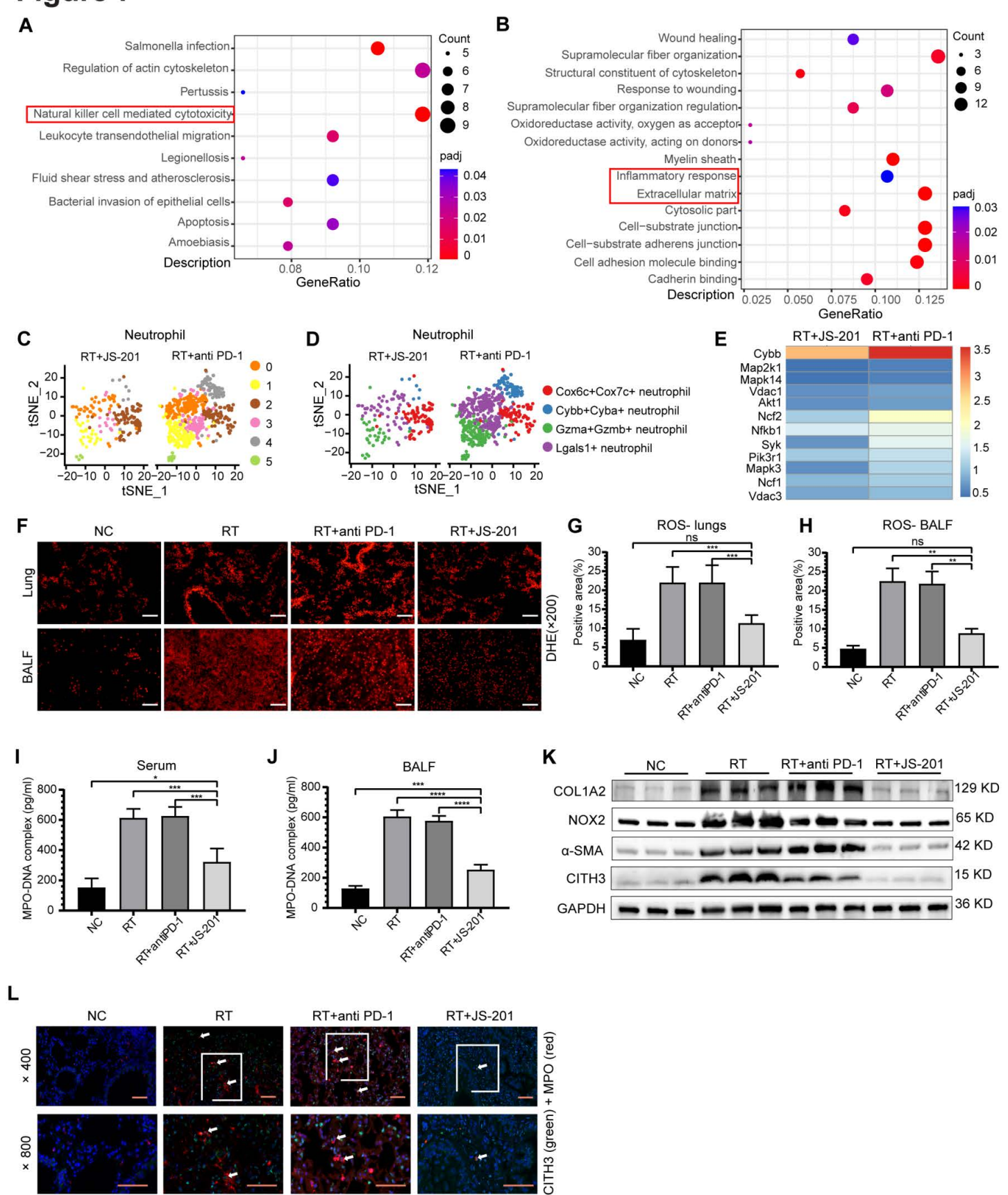












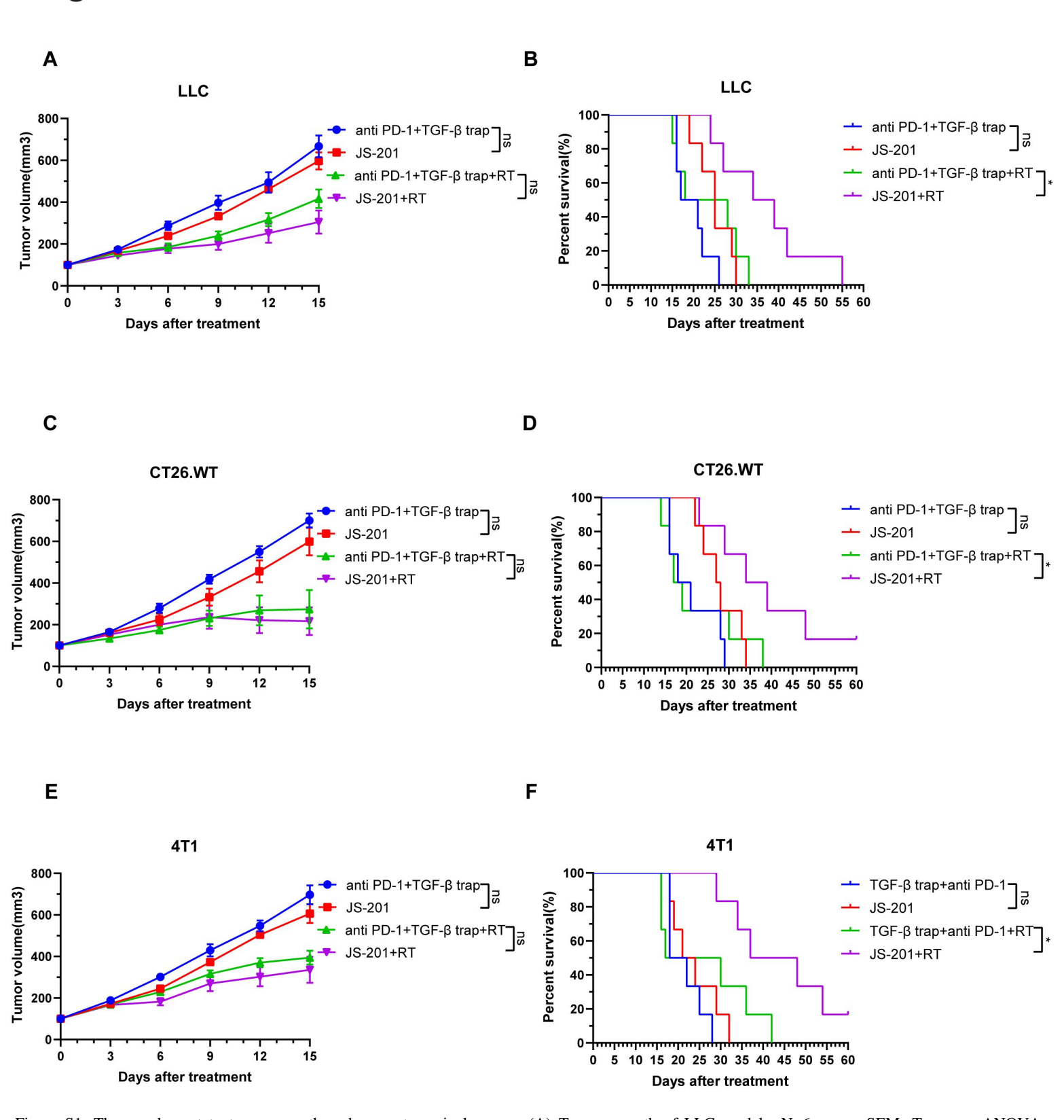


Figure S1. The supplement to tumor growth and percent survival curves. (A) Tumor growth of LLC models. N=6; mean±SEM; Two-way ANOVA analysis. (B) Survival curves of LLC models. N=6; Kaplan-Meier curves with Cox tests. (C) Tumor growth of CT26 models. N=6; mean±SEM; Two-way ANOVA analysis. (D) Survival curves of CT26 models. N=6; Kaplan-Meier curves with Cox tests. (E) Tumor growth of 4T1 models. N=6; mean±SEM; Two-way ANOVA analysis. (F) Survival curves of 4T1 models. N=6; Kaplan-Meier curves with Cox tests. *, p < 0.05; ***, p < 0.01; ****, p < 0.001; ****, p < 0.0001; ns, no significance.

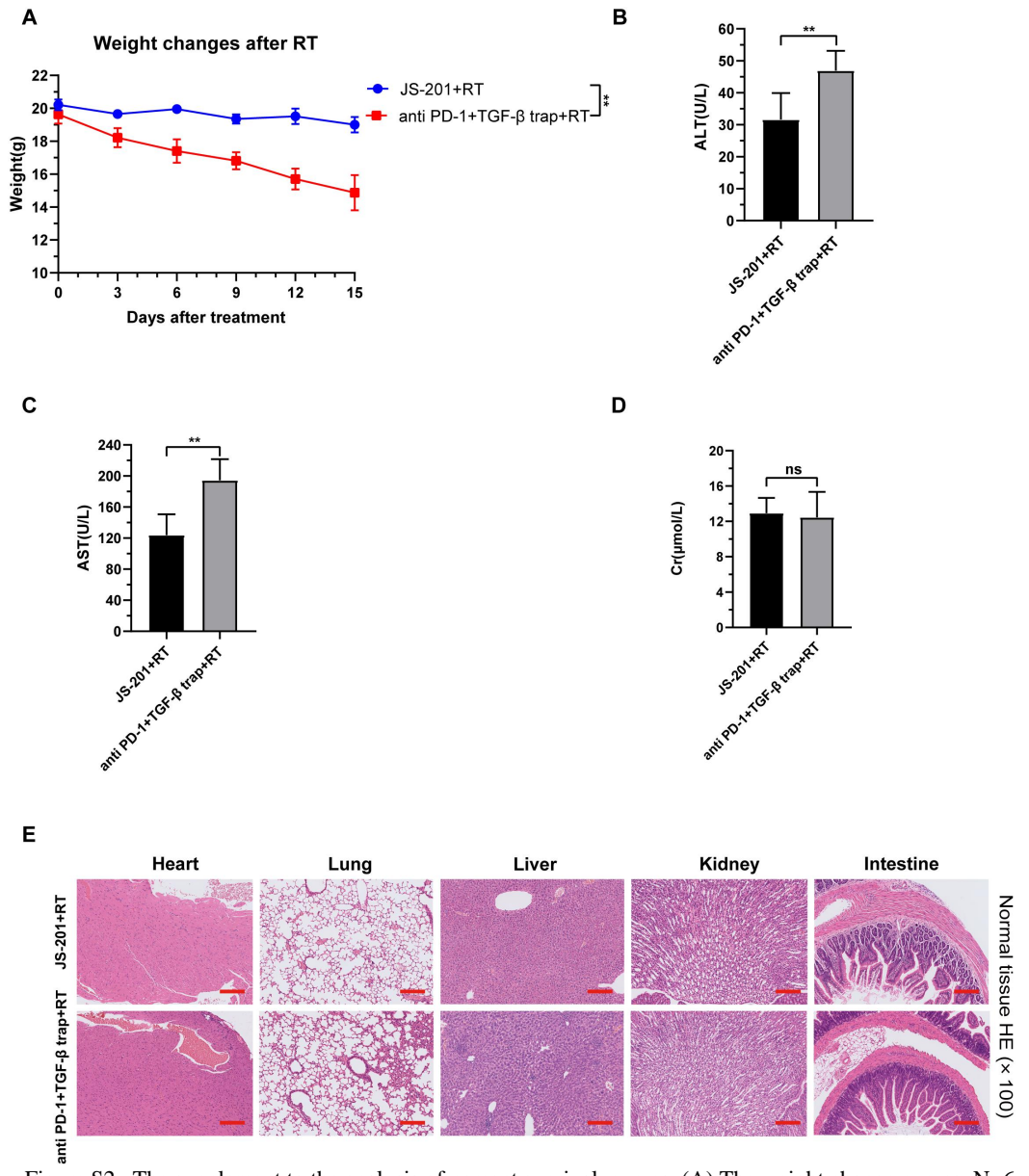


Figure S2. The supplement to the analysis of percent survival curves. (A) The weight change curves. N=6; mean \pm SEM; Two-way ANOVA analysis. (B) ALT, (C) AST, (D) Cr detection and (E) Normal tissue HE staining of JS-201+RT and anti PD-1+TGF- trap groups 15 days after treatment. N=3; mean \pm SD; paired Student's T test. *, p < 0.05; **, p < 0.01; ****, p < 0.001; ****, p < 0.0001; ns, no significance. The red scale bar is 200 μ m.

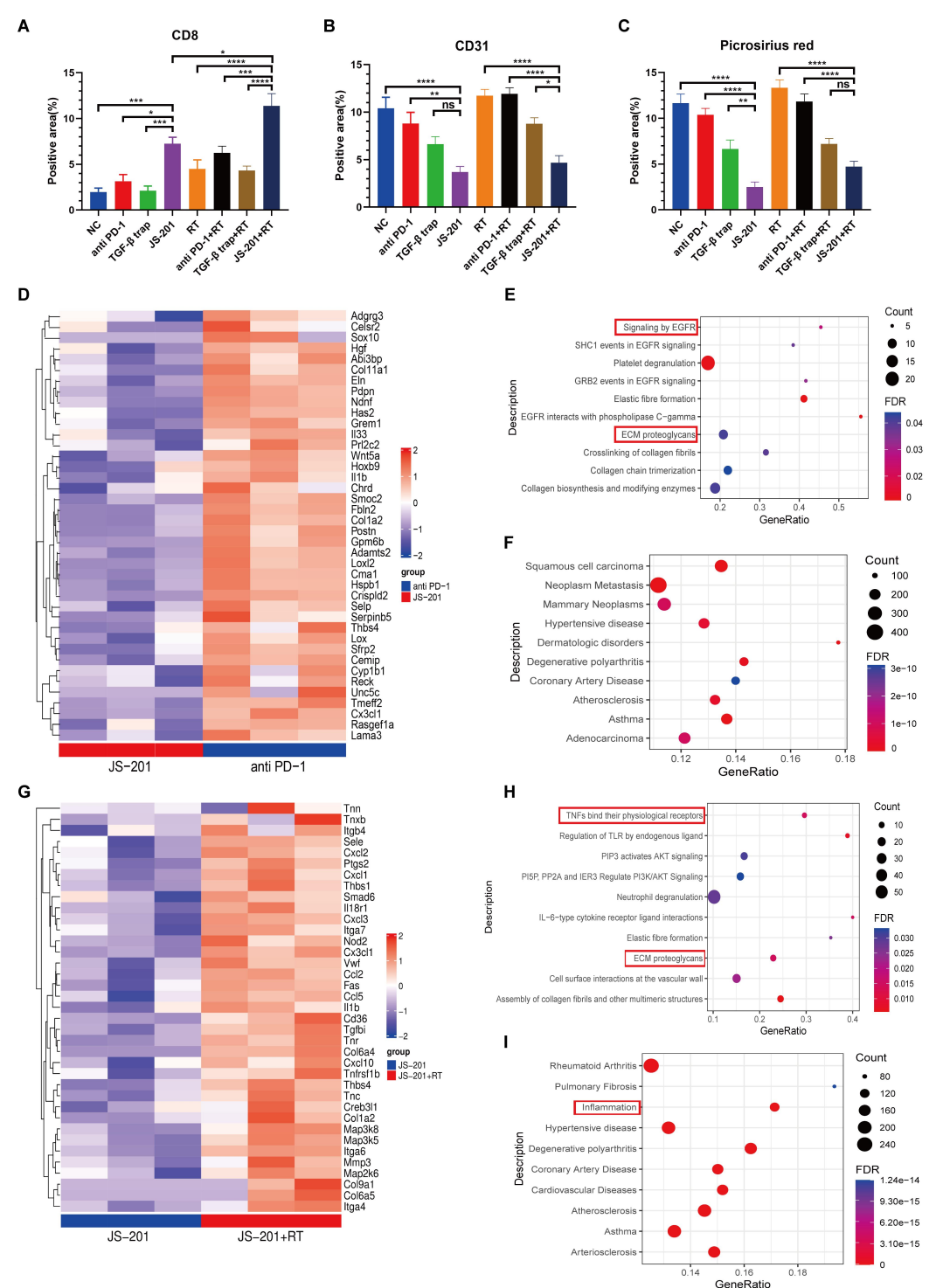


Figure S3. The supplement to IHC and RNA-Seq results of LLC tumor tissues. (A) Analysis of CD8, (B) CD31 and (C) picrosirius red staining of LLC tumors. N=3; mean \pm SD; One-way ANOVA analysis. (D) The heatmap, (E) Reactome, and (F) DisGeNET enrichment of down-regulated DEGs in LLC tumors treated with JS-201 compared to anti-PD-1. (G) The heatmap, (H) Reactome and (I) DisGeNET enrichment of up-regulated DEGs in LLC tumors treated with combination therapy compared to JS-201 alone. N = 3 . *, p < 0.05; **, p < 0.01; ****, p < 0.001; *****, p < 0.0001; ns, no significance.

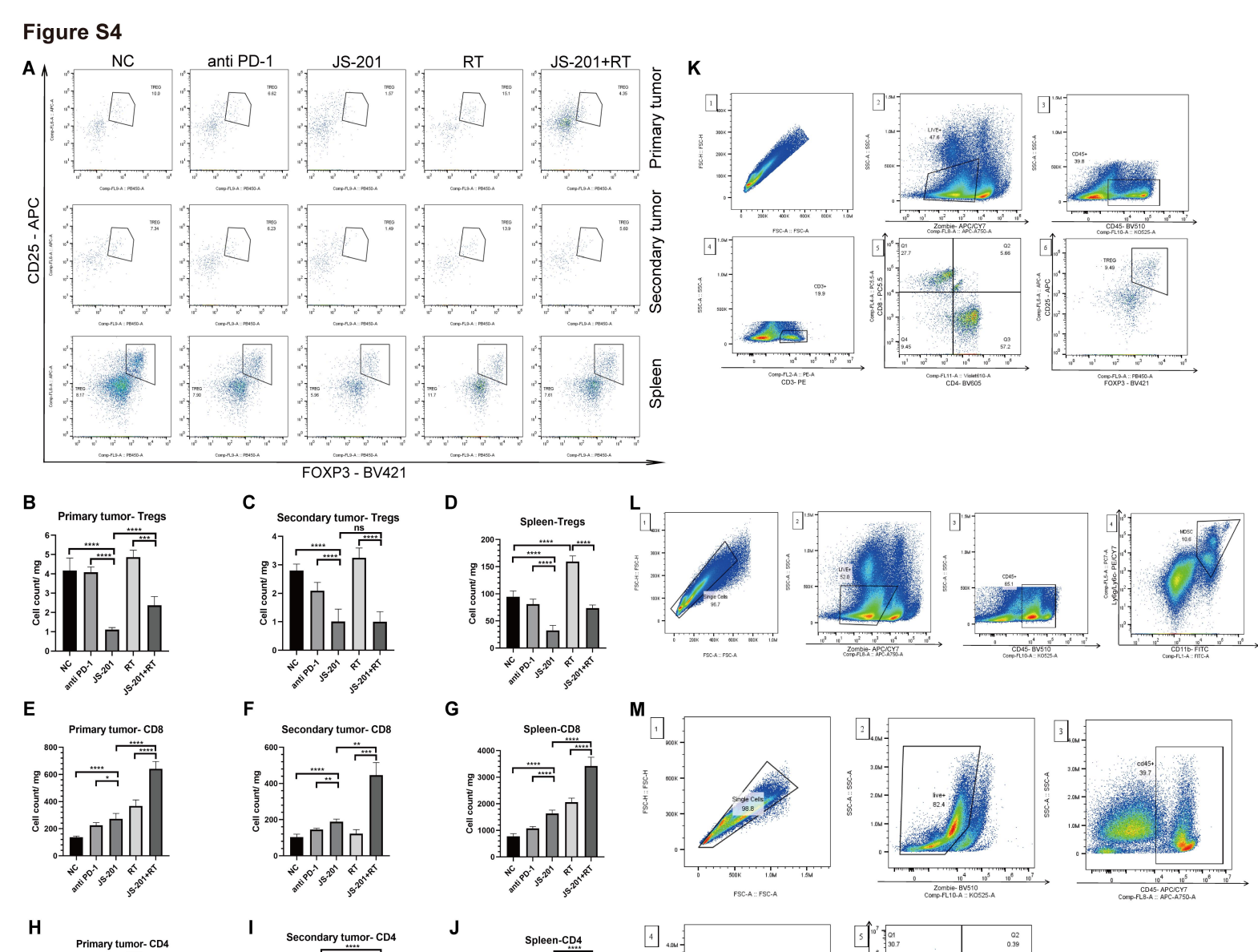


Figure S4. The supplement to flow cytometry. (A) Tregs in the primary tumors, secondary tumors and spleens. (B) The analysis of Treg amount per milligram of primary tumors, (C) secondary tumors and (D) spleens. (E) The analysis of CD8+ T cell amount per milligram of primary tumors, (F) secondary tumors and (G) spleens. (H) The analysis of CD4+ T cell amount per milligram of primary tumors, (I) secondary tumors and (J) spleens. N=3; mean \pm SD; One-way ANOVA analysis. (K) The gating strategy of Tregs, (L) MDSCs, (M) CD8+ and CD4+ T cells. *, p < 0.05; ***, p < 0.01; ****, p < 0.001; *****, p < 0.0001; ns, no significance.

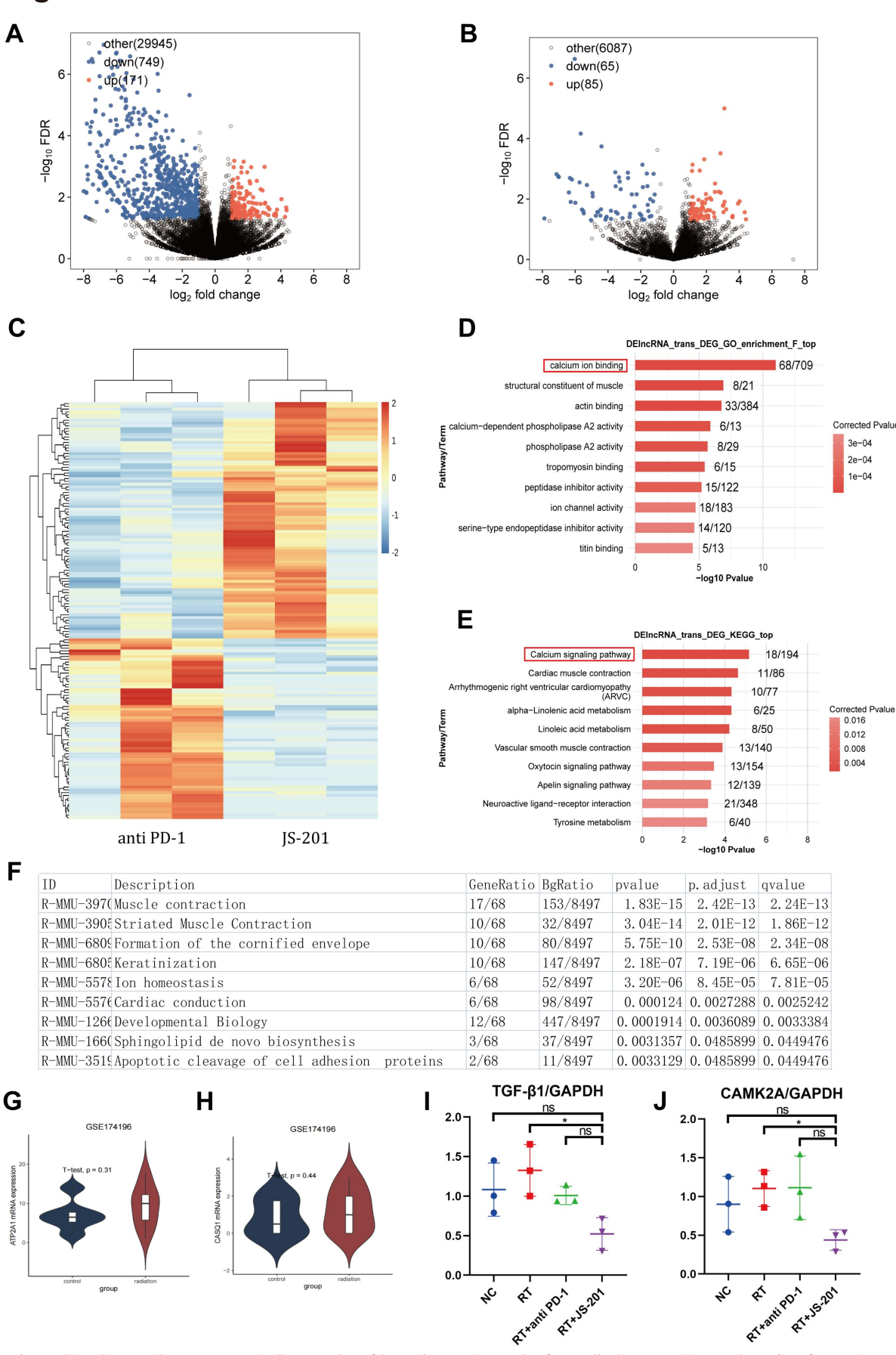


Figure S5. The supplement to RNA-Seq results of lung tissues 1 month after radiotherapy. (A) Total DEGs of mRNA between the JS-201 and anti-PD-1 groups. (B) Total DEGs of lncRNA between the JS-201 and anti-PD-1 groups. (C) The heatmap of significant DEGs of lncRNA between the JS-201 and anti-PD-1 groups. N=3. (D) GO and (E) KEGG enrichment of significant DEGs of lncRNA. (F) Reactome enrichment results of DEGs of mRNA. (G) ATP2A1 and (H) CASQ1 expression in GSE 174196 dataset. lncRNA, long non-coding RNA; mRNA, transcriptome RNA. (I) The density analysis of TGF- 1/GAPDH and (J) CAMK2A/GAPDH during RP. N=3; mean \pm SD; O n e - way ANOVA analysis. *, p < 0.05; **, p < 0.01; ***, p < 0.001; ****, p < 0.0001; ns, no significance.

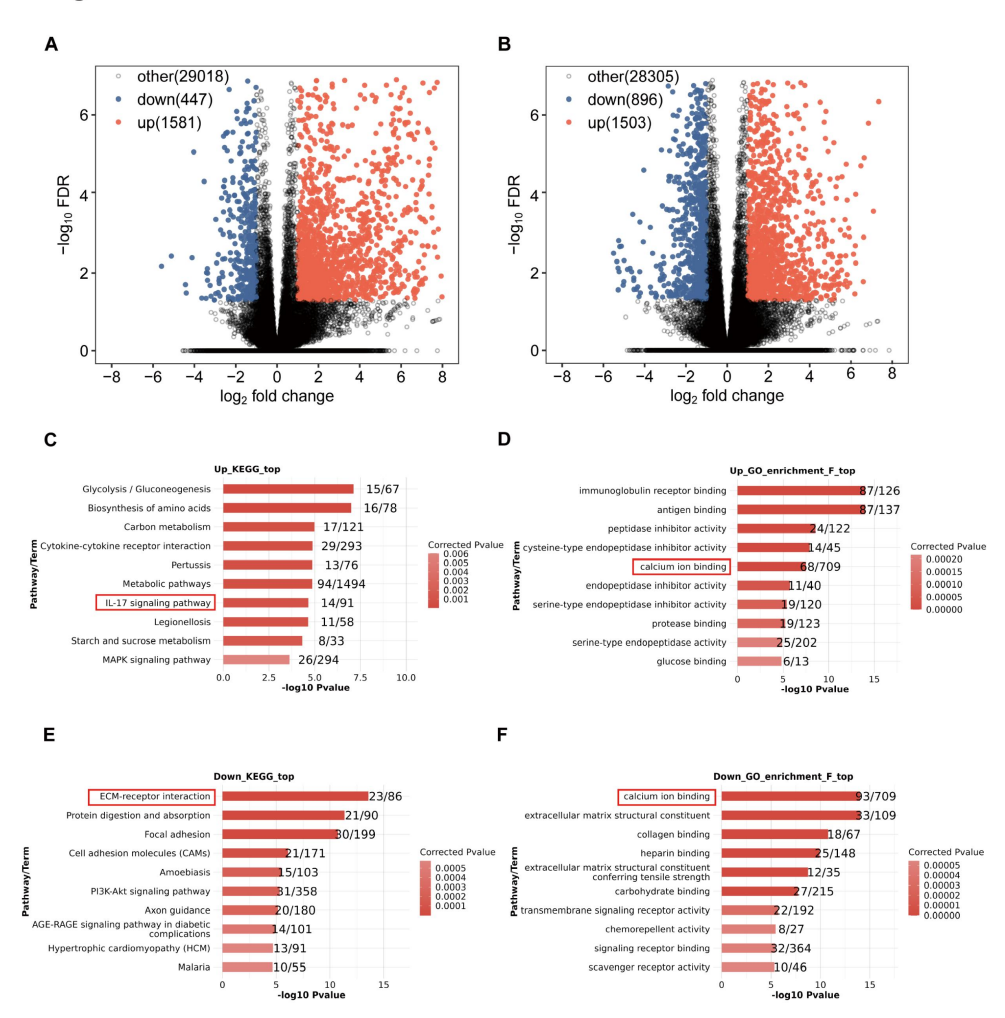


Figure S6. The supplement to RNA-Seq and analysis of mice lungs 1 month after radiotherapy. (A) Total DEGs of mRNA between the RT and anti-PD-1 groups. (B) Total DEGs of mRNA between the RT and JS-201 groups. N=3. (C) KEGG enrichment and (D) GO enrichment of up-regulated DEGs in the anti-PD-1 group compared to the RT group. (E) KEGG enrichment and (F) GO enrichment of down-regulated DEGs in the JS-201 group compared to the RT group.

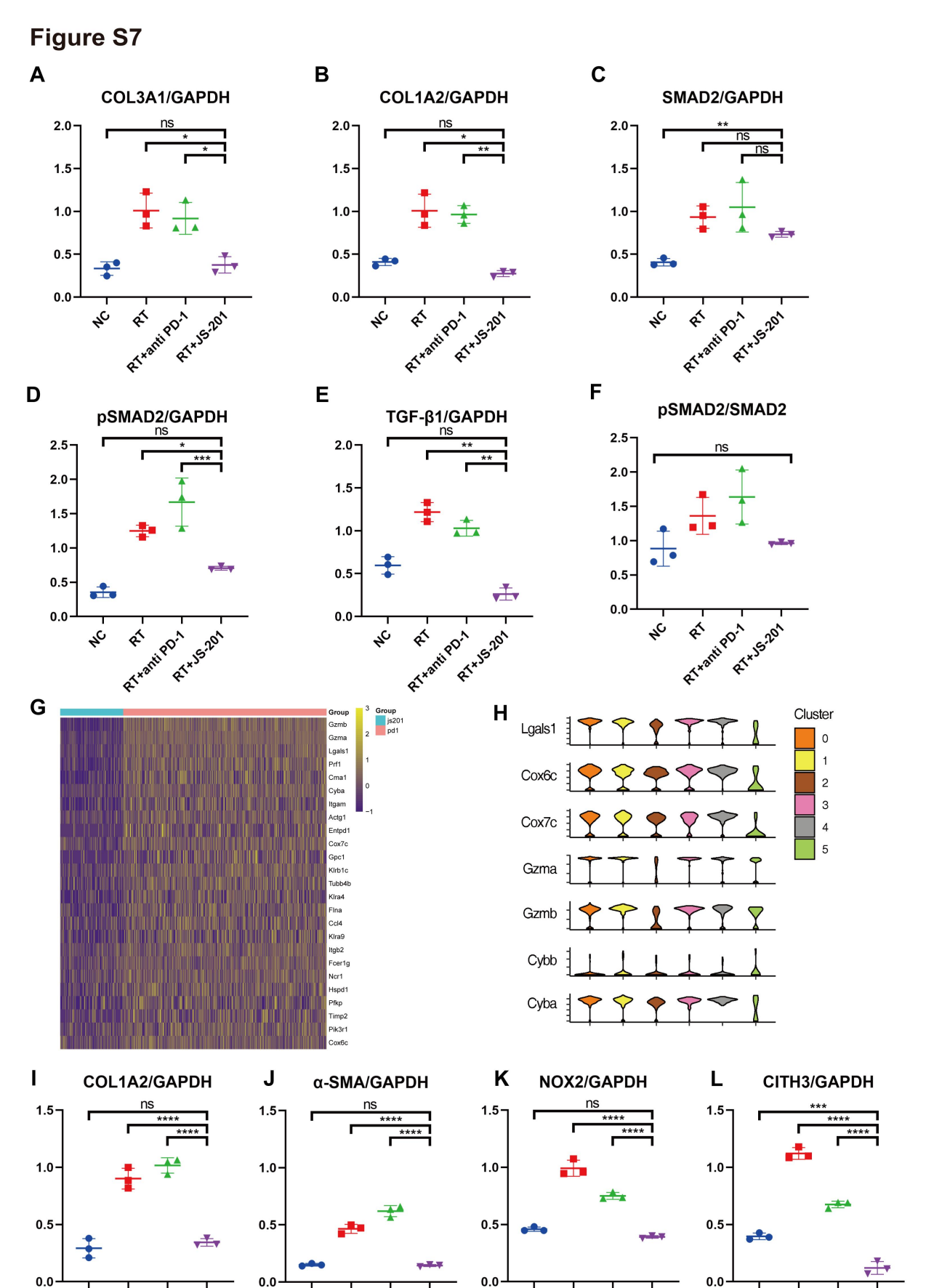


Figure S7. The supplement to single-cell RNA-Seq and WB results of lung tissues 6 months after RT. (A) The density analysis of COL3A1/GAPDH, (B) COL1A2/GAPDH, (C) SMDA2/GAPDH, (D) pSMAD2/GAPDH, (E) TGF- 1/GAPDH and (F) pSMAD2/SMDA2 during RIPF. (G)The heatmap of DEGs in neutrophils between groups. (H) The expression of Cox6c, Cox7c, Lgals1, Gzma, Gzmb, Cybb and Cyba in neutrophils. (I) The density analysis of COL1A2/GAPDH, (J) -SMA/GAPDH, (K) NOX2/GAPDH and (L) CITH3/GAPDH during RIPF. N=3; mean \pm SD; One-way ANOVA a n a 1 y s i s . *, p < 0.05; **, p < 0.01; ***, p < 0.001; ****, p < 0.0001; ns, no significance.

RT+artiPD.

λC

21*15:201

RT*antiPD.

4c

27*15:201

AT*antiPD.A

ď

27*35:201

AT*antiPD.

27*15:201

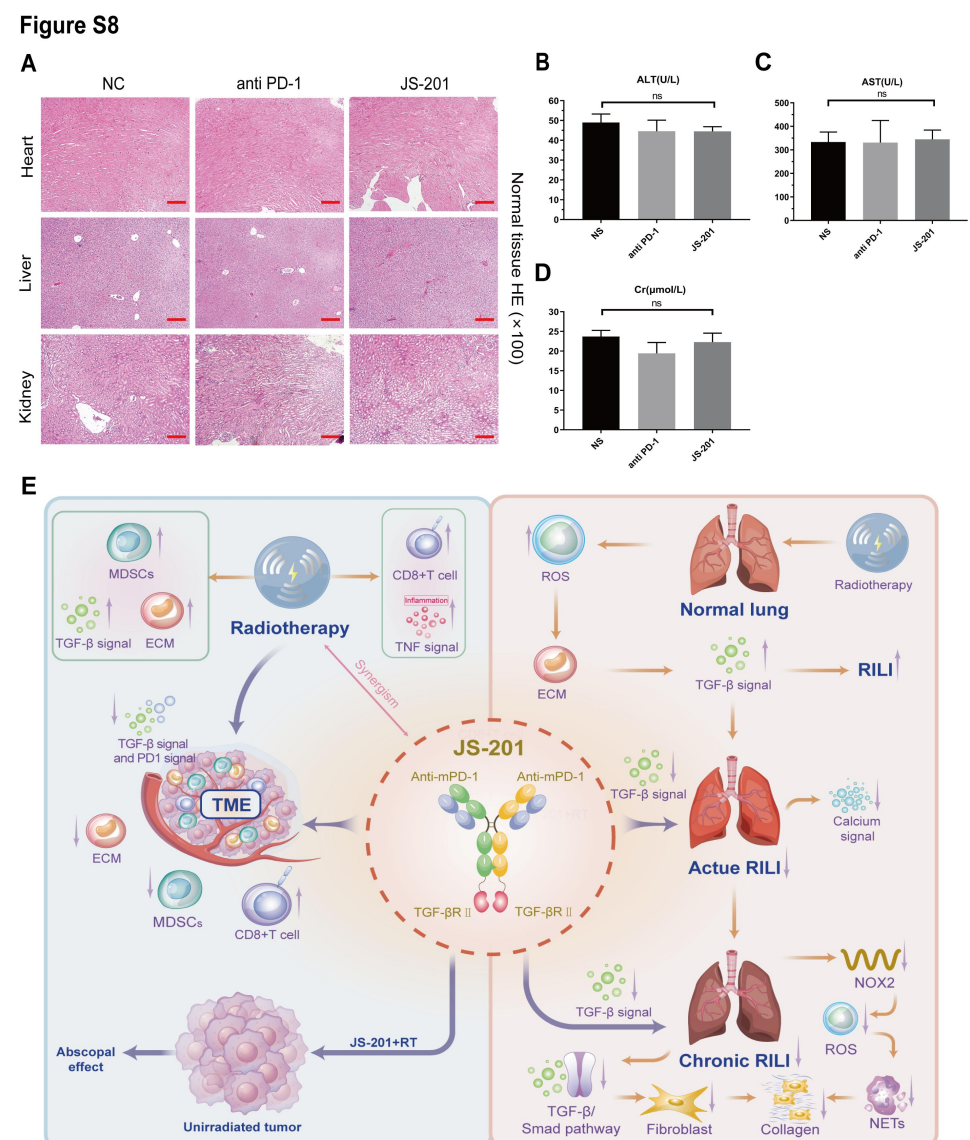


Figure S8. In vivo biosafety evaluation of JS-201 and summary of combination therapy. (A) HE staining of the heart, liver and kidney of mice. (B) AST, (C) ALT and (D) Cr levels in mouse serum. N=3; means ± SD; One-way ANOVA analysis. The red scale bar is 200 µm. (E) Summary of combination therapy. In the TME, JS-201 inhibits ECM production mediated by signaling and improves immune cell infiltration, including reducing MDSCs and increasing CD8+ T cells. RT has a bidirectional effect on the TME, enhancing the intratumor inflammatory response by upregulating CD8+ T-cell infiltration and TNF signaling while promoting MDSC and ECM production. JS-201 exerts synergistic effects with RT signaling, based targeting PD-1 and TGFand the combination demonstrates a significant abscopal effect. In acute RILI, JS-201 inhibited the calcium signaling pathway. In chronic RILI, JS-201 inhibits the TGF-/Smad pathway to reduce fibroblast proliferation and reduces ROS production by inhibiting NOX2, thereby relieving NET release and collagen production. AST, aspartate aminotransferase; ALT, alanine aminotransferase; Cr, creatinine; ECM, extracellular matrix; MDSCs, myeloid-derived suppressor cells; NETs, neutrophil extracellular traps; PD-1, programmed cell death protein-1; RILI, radiation-induced lung injury; ROS, reactive oxygen species; RT, radiotherapy; TGF-, transforming growth factor - ; TME, tumor microenvironment; TNF, tumor necrosis factor.

Cluster	Celltype	Marker
0	Macrophage 1	Cd86
1	T cell	Cd3e,Ptprc
2	Th2 cell	Gata3,Cd4,Cd3e
3	Th2 cell	Gata3,Cd4,Cd3e
4	T cell	Cd3e,Ptprc
5	Lipofibroblast	Plin2,Fabp4,Fabp5
6	Monocyte	Itgam,Cd14
7	Lipofibroblast	Plin2,Fabp4,Fabp5
8	Neutrophil	Itgam,Ptprc
9	Lipofibroblast	Plin2,Fabp4,Fabp5
10	Lipofibroblast	Plin2
11	Lipofibroblast	Plin2
12	Macrophage 1	Cd86
13	Progenitor cell	Ly6a
14	Endothelial cell	Pecam1,Cdh5
16	Macrophage 1	Cd86
17	Endothelial cell	Pecam1,Cdh5
18	Alveolar epithelial cell 1	Норх
19	Fibroblast	Pdgfra,Colla1
20	Progenitor cell	Cd34
21	Lipofibroblast	Plin2,Fabp4,Fabp5
22	Pericyte	Mcam,Pdgfrb
23	Macrophage 1	Cd86